Modelling visco-elastic source processes at Ngauruhoe Volcano, Central North Island, New Zealand

A. D. Jolly – GNS Science
P. Jousset
J. Neuberg
S. Sherburn – GNS Science
P. Smith

GNS Science Consultancy Report 2010/187
July 2010

GNS SCIENCE
TE PŪ AO

DISCLAIMER

BIBLIOGRAPHIC REFERENCE

Jolly, A.D.; Sherburn, S.; Jousset, P.; Smith; P., Neuberg; J. 2010. Modelling visco-elastic source processes at Ngauruhoe Volcano, Central North Island, New Zealand, *GNS Science Consultancy Report* 2010/187. 32p.

CONTENTS

TABLES

FIGURES

EXECUTIVE SUMMARY

Ngauruhoe volcano has produced repeated earthquakes since early 2006 with each earthquake exhibiting similar waveform features. These earthquakes are known to have slowly evolving source properties through time with spectral frequencies increasing during the period of observation (2006-2009). We have conducted a limited inversion for moment tensor components of an example low-frequency earthquake occurring 17 January 2008. Our inversion method is completed in two ways: 1) inversion for a non evolving source process, and 2) inversion for a time varying source process. For the non-evolving source inversion, we find that the moment tensor components match either a vertical pipe geometry or a vertical crack oriented either NE - SW or NW - SE. For the evolving source inversion, the earthquake onset fits a vertical pipe geometry, while the later stages of the earthquake coda fit a vertical crack oriented N - NE (along the volcanic axis). For earlier inversion runs, the best fit location was found at ~800 m below the volcano summit area. The volumetric moment tensor components are about 1 to 5 x 10^{11} Nm. The model fits the observations at the three closest stations (temporarily deployed seismometers) located within 1.5 km of the source, but not at more distant seismic stations (OTVZ, NGZ) which are >3 km from the source. This discrepancy is probably due to low velocities in the uppermost crust which are not represented in the velocity model. Additional model trials using an alternative low velocity surface layer (2.5 km/s instead of 3.3 km/s) yield improved fits to first arrivals at the further stations and underscore the uncertainties associated with the method. Alternative source models are not consistent with the waveform data. We also separately apply a new analytical approach to examine the role of damping in volcanic earthquake resonance. This approach shows that acoustic waves may be strongly damped within resonating cavities, while the associated interface waves dominating the low-frequency earthquakes, can have relatively low damping values, as long as the viscosity within the cavity is high. This result has implications for the estimation of the resonator properties which control the low-frequency earthquakes at Ngauruhoe.

1.0 INTRODUCTION

Ngauruhoe is located near the southern margin of the Taupo Volcanic Zone (TVZ) and is a small composite cone at the southern end of the Tongariro Volcanic centre (Figure 1). Ngauruhoe is one of the most active volcanoes in the TVZ producing small eruptions once every three years on average since 1840 (G. Jolly pers. comm.). It last erupted in 1974-75 with low level Vulcanian/Strombolian style eruptions. After the 1974-75 eruptions, Ngauruhoe entered a period of repose, producing virtually no seismicity and only very low level fumarolic activity. The system became more active in May 2006 when a series of small earthquakes were recorded on two permanent stations (NGZ and OTVZ). The new activity prompted *GeoNet* to increase the alert level code from Level 0 (dormant or quiescent state) to Level 1 (signs of volcanic unrest), to examine past data, and to increase monitoring by adding three new temporary seismic stations (NGA1, NGA2, NGA3). Evaluation of the earlier data showed that a small number of the same earthquakes were recorded as early as May 2005. The new stations offered the ability to find rudimentary earthquake magnitude estimates (Figure 2) and earthquake locations (Figure 3). The earthquakes were found to be located on the north flank of the volcano and about 1 km below the model surface. Uncertainties were reasonably large (> 1 km) for these locations however (Figure 3). Activity dropped to near background levels by May 2007 and then subsequently restarted in October 2007. The new activity prompted a second temporary deployment in January 2008 (NGA4, NGA5, NGA6) which were positioned over the inferred source location found in the 2006 deployment. The 2008 deployment produced an observation of a significant change in the spectral signatures of seismicity (Figure 4). The change occurred during the deployment and so was captured by 5 seismic sensors. Careful analysis of the waveform onsets for the two permanent stations showed that the relative position of the arrival times did not change at the time that the spectra changed. Hence the change is inferred to be due to source properties and not to a change in source position.

We selected a single event from this period (prior to the observed change) for detailed analysis. This event, and other earthquakes in the sequence, was found to contain significant low frequency energy (from 0.66 to 5 Hz) (Figure 4). By filtering this event from 0.33 to 1.0 Hz, we obtain a low frequency source response which might represent the fundamental properties of the source trigger and resonance. For this filtered set of waveforms, we obtained moment tensor components by application of a waveform inversion method (Nakano and Kumagai, 2005). We use this method to constrain both the possible source geometry and orientation for Ngauruhoe earthquakes.

We also offer a new analytical approach to understand damping of magmatic fluids in resonating sub-surface cavities. We demonstrate that interface waves established in these cavities experience less damping than acoustic waves traversing the fluid media, if the fluids have high viscosity. This work has implications for the interpretation of low-frequency seismicity in volcanoes like Ngauruhoe which show low-frequency earthquakes at very shallow depth, but no associated increase in degassing or deformation signals.

2.0 THEORY AND METHOD

2.1 Theoretical basis

In simple terms, the displacement response of a seismometer to a volcanic source perturbation is the result of moments (and/or forces if relevant) applied in some directional system (e.g. Cartesian coordinate system) after traversing the Earth and can be described (using the notation and theoretical development of Ohminato et al., 1998) by

$$u_n(t) = M_{pq}(t) * G_{np,q}(t),$$

$$p,q = x,y,z$$

where the displacement response $u_n(t)$ can result from the elastic response to a set of unidirectional impulses $G_{np,q}(t)$ of the Green tensor, and $M_{pq}(t)$, is the time history of the *pq* elements of the moment tensor, *n* is the component of displacement at the receiver, and ,*q* implies spatial differentiation with respect to the *q* coordinate.

The practical solution of the above problem is outlined in several papers (e.g. Ohminato et al., 1998) and comes down to discretizing the generalised equation

$$u_n(t) = \sum_{i=1}^{N_m} \int_{-\infty}^{\infty} m_i(\tau) G_{ni}(t-\tau) d\tau,$$

where N_m is the number of unique moment components m_i. We use $N_m = 6$ for unique moment components. Replacing the continuous variables *t* and τ with discretized forms

$$t = p\Delta t \qquad (p = 0,\ldots,N_s)$$

$$\tau = k\Delta\tau \qquad (k = 0,\ldots,N_\tau)$$

where Δt is the sampling interval, N_τ is the number of elementary functions used to represent the source time function and N_s is the number of samples, yielding the equation

$$u_n(p\Delta t) = \sum_{i=1}^{6} \sum_{k=1}^{Nt-1} M_i(k\Delta\tau) * G_{ni}(p\Delta t - k\Delta\tau)\Delta\tau$$

$$n=1,...,N_t$$

$$p=1,...,N_s$$

where *i* is the number of relevant moment tensors, $u_n(p\Delta t)$ is the displacement of a sample of the n*th* seismogram at time $t=p\Delta t$, $G_{ij}(p\Delta t - k\Delta\tau)\Delta\tau$ is the Green's function for the n^{th} trace due to the i^{th} source mechanism at time $p\Delta t$ time shifted by $k\Delta\tau$, and $M_i(k\Delta\tau)$ is the value of each moment component *i* time shifted by $k\Delta\tau$ and is derived from an elementary source time function. The * denotes convolution.

To obtain an understanding of source processes in volcanic systems, we solve the above discrete equation by first finding the Green's function (see section 2.2) and then convolving

this impulse response with reasonable moment components (see section 2.3) to obtain synthetic displacements which can be compared against observed displacements. We note that the discussion above is based on an elasto-dynamic theory of the Earth, while the volcanic system we are examining is probably visco-elastic in nature. We here assume that the visco-elastic response to a uni-directional impulse can be faithfully represented in the same manner as the elasto-dynamic response developed in the theory above.

2.2 Modelling seismic wave propagation in complex media with topography

Several modelling methods for wave propagation, which take attenuating and dispersion effects into account have been proposed (Carcione, 1993; Carcione et al., 2002). We use a 3-D version of a finite-difference velocity-stress time domain formulation (Virieux, 1986; Levander, 1988; Graves, 1996) of the viscoelastic wave equations (Robertsson et al., 1994), in a heterogeneous medium with a non-flat free-surface topography (Hestholm & Ruud, 2000). This formulation comprises (i) the P-SV equation of motion; (ii) constitutive laws; (iii) equations for memory functions. We consider an array of standard linear solids (SLS) as a model for the frequency dependent viscoelastic rheology of volcanic media (Jousset et al., 2004).

The incorporation of surface topography is achieved by using a linear mapping transformation (Figure 5) of the rectangular computational grid into a curved grid (Tessmer et al., 1992). The 2-D mapping function can be written as

$$x(\zeta,\eta) = \zeta$$
$$z(\zeta,\eta) = \frac{\eta}{\eta_{\max}} z_0(\zeta)$$

where $z_0(\zeta)$ is the topography function, and the rectangular (ζ,η)-system is bounded by ζ=0, ζ=ζmax, η=0, η=ηmax. For curved profile (x,z) system, the extent of stretching is proportional to the distance from the bottom edge of the grid. For any F(x,z) function representing the distribution of any physical property or field in the medium, the equations for the linear mapping transformation are

$$\frac{\partial F}{\partial x} = \frac{\partial F}{\partial \zeta} + A(\zeta,\eta)\frac{\partial F}{\partial \eta}$$
$$\frac{\partial F}{\partial z} = B(\zeta)\frac{\partial F}{\partial \eta}$$

where ζ, η are the coordinates in the computational grid (Hestholm & Ruud 2000; Ruud & Hestholm 2001). In our case, linear mapping transformations are made considering 3-D. ξ is transformed in y in the same way as ζ is transformed in x.

2.3 Moment component analysis

Our approach follows closely that of Nakano and Kumagai (2005) who found that stable moment tensor inversion results could be obtained with as few as 3 seismic stations if the point source models were limited to the simplest yet realistic source geometries that might be observed in the volcanic environment.

We use the visco-elastic method outlined above (Section 2.2) to calculate uni-directional Green's functions for relevant moment tensor components within the Cartesian coordinate system described in Figure 6. These components are convolved with the 9 moment tensor components (M_{xx}, M_{yy}, M_{zz}, $M_{xy}=M_{yx}$, $M_{xz}=M_{zx}$, $M_{yz}=M_{zy}$). The moment tensor components can be found for simple geometric systems (e.g., Chouet, 1996) that are particularly relevant to volcanic environments and include:

Crack geometry

$M_{xx} = M_o(\lambda/\mu + 2\sin^2\theta\cos^2\varphi)$

$M_{xy} = M_{yx} = M_o(2\sin^2\theta\sin\varphi\cos\varphi)$

$M_{xz} = M_{zx} = M_o(2\sin\theta\cos\theta\cos\varphi)$

$M_{yy} = M_o(\lambda/\mu + 2\sin^2\theta\cos^2\varphi)$

$M_{zy} = M_{yz} = M_o(2\sin\theta\cos\theta\sin\varphi)$

$M_{zz} = M_o(\lambda/\mu + 2\cos^2\theta)$

Pipe geometry

$M_{xx} = M_o(\lambda/\mu + \cos^2\theta\cos^2\varphi + \sin^2\theta)$

$M_{xy} = M_{yx} = M_o(\sin^2\theta\sin\varphi\cos\varphi)$

$M_{xz} = M_{zx} = -M_o(\sin\theta\cos\theta\cos\varphi)$

$M_{yy} = M_o(\lambda/\mu + \cos^2\theta\sin^2\theta + \cos^2\varphi)$

$M_{zy} = M_{yz} = -M_o(\sin\theta\cos\theta\sin\varphi)$

$M_{zz} = M_o(\lambda/\mu + \sin^2\theta)$.

Isotropic source

$M_{xx} = M_{yy} = M_{zz} = M_o(\lambda + 2\mu)$,

where λ and μ are elastic Lame parameters, and the angles θ and φ are shown in Figure 6. We obtain trial moments $M_o = S(t)\,\mu\,\Delta V$ from the above set of geometries by combining a fundamental source time function S(t) and an incremental volume change $\Delta V = S(t)^* \Delta A$. We use $S(t) = 1-\cos(t/t_p)$, where t is time and t_p is the period of the source time function. We tried several t_p and found t_p =0.4 s gave stable waveform inversion results. We assume λ = μ = 0.5×10^{11} N/m^2 (Turcotte and Shubert, 1982) assuming a Poisson ratio of 0.25 (a value commonly used in volcano source modelling studies (Nakano and Kumagai, 2005). The fundamental source time function (related as moment) was then convolved with a pseudo-impulse response obtained for each fundamental moment tensor orientation (using the 3DFD

method outline in section 2.2) producing a synthetic output waveform. Each output waveform (for the geometries outlined above) were then compared to observed data for the 5 stations (15 components). To compare unambiguously the results for crack, pipe and isotropic geometries we need to account for different free parameters for the different geometries. We used the Akaike Information Criterion (Akaike, 1974; Nakano and Kumagai, 2005) to test the various models.

$$AIC = N_t N_s \ln(Err) + 2 N_f$$

Where *Err* is the residual, N_t is the number of waveforms, N_s is the number of samples in each waveform, and N_f is the number of free parameters. We use $N_f = N_t$ for a horizontal crack and pipe, and $N_f = N_t + 1$ for a vertical crack (Nakano and Kumagai, 2005). For each trial source geometry and orientation, we compare the observed and computed wavelets and determine the misfits (*c.f.* Jolly et al., 2010) at each time step Δt. We then construct a source time history by generating a series of time-shifted sub-events. Each sub-event is generated by convolution of fundamental Green's functions with the elementary seismic moment function M_o. Our implementation is similar to the method developed by Kikuchi and Kanamori (1982, 1986, 1991).

We try two approaches for our implementation. In approach A we assume that the source geometry, or the subsequent resonance, does not change through time. Hence the amplitude of the moment tensor components will change through time but not relative to each other. In approach B, we allow the source geometry to change through time and hence we can examine how the energy is dissipated from the source onset through to the event coda. In the case of a volcanic earthquake, approach B might allow us to distinguish if the earthquake trigger geometry was different from the resonator geometry.

An important point arises in regard to the model inversion approach and the minimization of errors. Our error estimation method will tend to accommodate the largest signals in preference to smaller signals (*c.f.* Ohminato et al., 1998). This means that closer stations, having bigger amplitudes, will contribute more to the error estimate than more distant stations. For an individual seismogram, the earlier high amplitudes will contribute more to the error estimation than the later low amplitude portions of the signal. In the case of modelling approach A, the best fit model will tend to fit the first few cycles of the closest station, with the late stage coda and more distant stations having less influence. For modelling approach B, the largest amplitude at any time step will still dominate, but the later coda of the earthquake will have as much weight as the earlier earthquake onset. With approach B it is critically important that phases match for closer and more distant stations. If for example, the velocity structure is mis-modelled, then amplitudes of close stations may be erroneously compared to unrelated phases at more distant stations. We discuss these issues in more detail in Section 3.

2.4 Model implementation

We applied a base 1D velocity model from Rowlands et al., (2005) for our initial modelling (Table 1). The flat layer for this model is distorted by the topography transformation method outlined above, but produces a useful approximation of the wavefield in volcanic environments (e.g. Jousset et al., 2004; Lokmer et.al, 2008; Jolly et al., 2010). We also tested an alternative low velocity model (see Section 3) (Table2) to learn about its role in the source inversion results.

We also conducted an analysis of damping (Table 3-6). These trials highlighted the uncertainties with application of waveform inversion techniques in regions where velocity and attenuation structures are unknown. Results for the low velocity model fit to our observations at stations OTVZ and NGZ.

To obtain stable waveforms within the frequency of interest, we used a grid spacing of 100 m laterally and 50 m in depth. This choice provided stable waveforms throughout the model area and allowed inversion of 1.5 second signals observed for the example event. Given the velocity model used in this study, and the frequency of interest (0.66 Hz), we assume the wavelength as ~0.75-1.5 km, giving 75 to 150 grid points per wavelength (within the numerical stability criterion outlined for the FD method) (Jousset et al., 2004). A summary of the computational setup is shown in Table 7.

The Green's functions produced by the FD implementation would ideally be generated from a delta pulse consisting of all frequencies. However, the finite grid size dictates an upper frequency limit. To obtain a stable impulse response, we used a Gaussian pseudo-impulse having a duration of 1 s within a 3 s window with a band limited frequency range. This choice matches closely the lowest frequencies observed in the data and is within the stability requirements dictated by the FD method at the chosen grid spacing.

2.5 Damping in volcanic systems

Assuming that low frequency earthquakes are generated by the seismic resonance in volcanic systems where fluids (hydrothermal, magma or gas) are embedded in an elastic solid, the amplitude decay can be described by

$$Q_a^{-1} = Q_i^{-1} + Q_r^{-1}$$

where Q_r^{-1} describes the energy loss by radiation of the resonating system and Q_i^{-1} represents the energy decay through anelastic damping in the magmatic fluid. The estimation of Q_i^{-1} could provide information about the properties of magmatic fluids such as viscosity, gas content crystal contents etc.

The seismic resonance is controlled by seismic interface waves at the solid-fluid boundary rather than acoustic P- waves travelling through the fluid (Ferazzini and Aki, 1987; Neuberg et al., 2000). The damping of acoustic P-waves is generally described by

$$Q_{aco}^{-1}(\omega) = \frac{\omega(\zeta + \frac{4}{3}\eta)}{\rho_f c_p^2}$$

where ω is the frequency, ζ is volume viscosity, η is the shear viscosity ρ_f is the fluid density and c_p is the acoustic velocity in the absence of any viscosity. While this equation is based on the Kelvin-Voight rheology model, the frequency dependence of damping in section 2.2 is controlled by an array of SLS used in our finite difference modelling. However Korneev (2008) has shown that the interface waves guided in a fluid filled container encounter an intrinsic damping described by

$$Q_{\text{int}}^{-1}(\omega) = \tan\left(\frac{1}{3}\tan^{-1}\left(-\frac{1+\sqrt{\frac{h^2\omega\rho_f}{72\eta}}}{\left(\frac{h^2\omega\rho_f}{12\eta}+\sqrt{\frac{h^2\omega\rho_f}{72\eta}}\right)}\right)\right)$$

where *h* is the width of the fluid filled container. Note that the damping of interface waves depends only on the shear viscosity while the acoustic damping depends on both shear and volume viscosity.

A comparison between the two damping mechanisms is depicted in Figure 7. For seismic frequencies, interface waves are damped far less than acoustic waves, for viscosities in the range of 10^7-10^9 Pas. Hence when dealing with interface waves, we need to map Q_{aco}^{-1} into Q_{int}^{-1}, if we want to infer from the damping of seismic waves about properties of magmatic fluids.

3.0 RESULTS

We limited our inversion to a small search domain around Ngauruhoe and within the computational domain summarised in Table 7. We first calculated Green's functions in a coarse spatial grid (500 m spacing, 5 nodes NS, 5 nodes EW and 3 nodes at 500, 100, and 1500 m giving 75 total coarse position computations). The inversion from these Green's functions produced a best fit solution directly beneath the volcano summit at 500 m depth. Next we computed Green's functions within a limited fine grid (an additional 30 models) about this coarse minimum solution, finding the best fit solution at a position located 200 m E, 100 m S and 800 m deep, relative to the volcano summit station NGA4, located within the outer moat of Ngauruhoe summit. At this position, and using the fixed geometry (approach A) outlined in Section 2.3, we found two vertical crack models with low misfit to the data. These models were oriented either N73^{o}W (Figure 8) or N46^{o}E (Figure 9) and produce similar source time functions (Figure 8f and 9f). We also found a low misfit example of a vertical pipe (Figure 10) model having a radially symmetric excitation. The geometries shown produced reasonable fits to the three temporary stations in the network (NGA4, NGA5, NGA6) but produced generally poor matches to the most distant stations (OTVZ and NGZ), a result which suggests that the base velocity model may be incorrect.

Because the calculated seismograms appeared to arrive ahead of the observed seismograms at stations OTVZ and NGZ, an alternative low velocity model may be more appropriate. To test this hypothesis, we calculated Green's functions for a slower velocity model (Table 2), assuming the same source time function shown in Figure 10. The low velocity trial produced somewhat better first arrivals to the more distant stations (compare Figure 10 d and e to Figure 11 d and e) but did not match the later phases well.

We also examined the role of attenuation in our modelling. Results of the application of alternative damping models are illustrated at station NGZ (Figure 12) from separate trials outlined in Tables 2-6. Note that for progressively higher damping, the amplitudes are progressively diminished and the phase arrival time are shifted to an earlier time. We note here that the highest damping values tested (*Q* = 50; Table 6) produced unstable waveforms and were not plotted. Also note that the first arrival for the synthetic explosion shows a

counter intuitive down first motion. Tests which included a deeper synthetic source (results not shown) yielded up first motions on the local stations, consistent with the expectation for an explosive source. We surmise that the down first motion (Figure 12) probably result from the effects of the velocity model and topography on the very shallow source.

The velocity and attenuation tests show that knowledge of both the velocity and attenuation structure is critical for a well constrained inversion for source properties (consistent with earlier papers (e.g. Lokmer, 2007)). We note that Rowlands et al. (2005) found that their highest layer (0 km depth) is reasonably constrained at Ngauruhoe, but we surmise that the velocities above sea level, and composing a large part of our model space, are probably not well constrained. We conclude from these tests that an attempt to find both the optimised velocity/attenuation structure and information about the source orientation would be very difficult given the discrepancy in arrival times and phases for near and more distant stations. We do, however, think that useful information about the source process can be obtained by focusing on the three nearest stations (NGA4, NGA5, NGA6) where phase mismatches are unlikely owing to the close proximity of the stations to the source.

Up to this point, we have considered geometric source models which do not change with time, and have outlined problems with matching data from close and more distant stations. However, we can also consider the possibility that the source geometry has changed as the event proceeds. This might happen if, for example, the event trigger subsequently excites a resonator having a different geometry.

We test this hypothesis, by relaxing our earlier modelling approach, and allowing the source geometry to change with time (i.e. we now apply approach B discussed in Section 2.3). Because we have known uncertainties in velocity and damping structure, we use only the three closest stations and use the location found in our earlier spatial search (i.e. 200 m East, 100 m South and 800 m below the summit of Ngauruhoe). From this procedure, we obtain a new set of waveform matches (Figure 13a,b,c) to the inverted source time function (Figure 13d). The waveform matches are only marginally different from those obtained using the fixed model approach (Figure 8, 9 and 10), but an analysis of time dependent errors (Figure 14) reveal that subtle source geometry changes occur with time (Figure 13d). The earliest part of the waveforms fit a vertical pipe having volumetric components from a [2,2,1] source (cyan peaks at less than 6 seconds in Figure 14). The model then shifts to a pipe orientation dominated by excitation of M_{yy} component (red peaks at 5 to 7 seconds). The latest stages of the inversion fit generally a North to North East crack orientation (> 7 s). A caveat must be applied to the interpretation of Figure 14 with regards to the interpretation of the change in excitation for the vertical pipe. The calculated Green's functions have fairly strong phase differences depending on the associated moment contributions. These phase differences might allow the inversion to resolve separate models from matches of the same data peaks. Regardless, the inversion provides a reasonable fit to the close seismic stations, and result in a source orientation which can be interpreted in the context of the Ngauruhoe volcanic system.

4.0 DISCUSSION

We obtain a new understanding of the properties of repeating earthquakes at Ngauruhoe through an analysis of waveform matching to reasonable source models. We find that source modelling is complicated by uncertainties in both the velocity and attenuation

structure. Regardless, we obtain an improved understanding of the source process and orientation which fits into the local volcano context and also the regional tectonic system.

The results suggest that the source onset is produced by the initial excitation of a vertical pipe (Figure 6 and 14) having equal magnitude moment components (M_{xx} and M_{yy}). The pipe structure might represent a portion of the long lived Ngauruhoe volcanic conduit which might still transport heat, gas and liquids from depth. Interestingly, the best fit crack model in Figure 14 trends N^{o}15 to 35^{o}E consistent with both the faults within and bounding the TVZ and also the orientation of volcanic vents (see Figure 1).

Given the model inversion, we suggest that the source trigger for each earthquake occurs due to repeated excitation of a vertical pipe geometry overprinted by a crack oriented approximately N15^{o} to 35^{o}E. The initial trigger might be due to fluid flow within a pipe shaped constriction while the later stages might be due to the subsequent resonance of a low impedance contrast crack.

If we consider that the geometry of the source process might have changed as the volcanic earthquake progresses, we must also consider the possibility that the position of excitation might change through time. Jousset et al., (2004) studied this phenomenon using a finite–difference method by initiating a trigger within an extended resonator. They found that the spatial focus of energy dissipation changed with time, with the initial source of energy dissipation centred at the trigger point but later stages shifting to the 'energy leaking' parts of the resonator body. If such a system occurred in nature, the best approach for finding both the trigger and 'leaky' resonator would be to invert for variable source processes in both a temporal and spatial sense.

Our analytical development of damping in fluids suggests that extended resonance can occur if the viscosity of the medium is sufficiently high. This has direct implications for hazards where resonating volcanic earthquakes are found because gas rich volcanic magma may belong to the class of materials which produce volcanic resonance.

5.0 FUTURE WORK

We have successfully inverted for fundamental source properties at Ngauruhoe volcano. We have also developed a new understanding of how damping occurs in resonant bodies. We next plan to examine in greater detail, the uncertainties associated with our inversion method. We will examine the role of alternative velocity models and variations in elastic parameters. It might also be useful to invert for the two distant stations (NGZ and OTVZ) with the caveat that cycle skipping may produce strongly ambiguous results.

We also plan to invert additional sample events recorded at Ngauruhoe. This work will focus on source property variations that might produce the observed changes in waveforms and spectra (Figure 4). This process should be straight forward because the source location is known to be fixed through time based on our earlier analysis (see Section 1). Hence we need only to recalculate 1 set of Green's functions, using a new pseudo-impulse response having an appropriate alternate frequency, and then inverting for the new source properties. Finally, we will plan to incorporate new attenuation estimates for the Tongariro region to improve our source modelling.

6.0 CONCLUSIONS

We have determined a new source geometry for local earthquakes recorded beneath Ngauruhoe volcano between 2005 and 2009 on a local 5 station seismic network using the inversion technique of Nakano and Kumagai (2005). We used a visco-elastic 3D finite difference method incorporating topography to obtain Green's functions for the local stations. These Green's functions are convolved with a realistic moment tensor solution to obtain synthetics for inversion against observations at 5 local stations. The results suggest that a vertical pipe geometry dominates the onset of the earthquake, while the later stages of the event are explained by a N15^{o} to 35^{o}E crack. We also separately develop a new analytical approach to understand the role of viscosity on damping in resonating fluid bodies.

7.0 REFERENCES

Akaike, H., 1974, A new look at the statistical model identification, IEEE Trans. Autom. Control, 9, 716-723.

Carcione, J.M., 1993, Seismic modelling in viscoelastic media, Geophysics,110-120.

Carcione, J.M., Herman, G.C. and ten Kroode, A.P.E., 2002, Seismic modelling, Geophysics, 67(4), 1304-1325.

Cassidy, J., Ingam, M., Locke, C. and Bibby, H., 2009, Subsurface structure across the axis of the Tongariro Volcanic Centre, New Zealand, J. Volc. Geotherm. Res., 179,233-240.

Chouet, B., 1996, New methods and future trends in seismological volcano monitoring, in Monitoring and Mitigation of volcano hazards, by R. Scarpa and R. Tilling, pp. 23-97, Springer, New York.

Ferrazzini V. and Aki, K., 1987, Slow waves trapped in fluid-filled infinite crack: implications for volcanic tremor, J. Geophys. Res., 92(B9), 9215-9223.

Graves, R.W., 1996. Simulating seismic wave propagation in 3D elastic media using staggered-grid finite differences. Bull. Seis. Soc. of Amer.; 86; 4; 1091-1106.

Grindley, G.W., 1960, Sheet 8 Taupo (1st edition) Geological map of New Zealand. Dept of Scientific and Industrial Research, Wellington, New Zealand.

Hestholm, S. and Rund, B., 2000, 2D finite-difference visco-elastic wave modelling including surface topography, Geophys. Prospect., 48, 341-373.

Jolly A.D., Sherburn, S., Jousset, P. and Kilgour, G., 2010, Eruption source processes derived from seismic and acoustic observations of the 25 September 2007 Ruapehu eruption-North Island, New Zealand, J. of Volc. Geotherm. Res., 191 (2010) 33–45.

Jousset, P., Neuberg, J. and Jolly, A., 2004, Modelling low frequency volcanic earthquakes in a viscoelastic medium with topography, Geophys. J. Int., 159, 776-802, doi:10.1111/j.1365-246X.2004.02411.x, 2004.

Kikuchi M. and Kanamori, H., 1982, Inversion of complex body waves, Bull. Seismol. Soc. Amer., 72, 491-506.

Kikuchi, M. and Kanamori, H., 1986, Inversion of complex body waves II, Phys. Earth Planet Inter., 43, 205-222.

Kikuchi, M. and Kanamori, H., 1991, Inversion of complex Body waves III, Bull. Seismol. Soc., 81, 2335-2350.

Korneev, V., 2008, Slow waves in fractures with viscous fluid, Geophysics 73(1), doi:10.1190/1.2802174.

Levander, A., 1988, Fourth-order finite-difference P-SV seismograms, Geophysics, 53, 1425-1436.

Lokmer, I., Bean, C., Saccorotti, G. and Patane, D., 2007, Moment tensor inversion of LP events recorded on Etna in 2004 using constraints obtained from wave simulation tests, Geophys. Res. Letts., 34, L22316, doi:10.1029/2007GL031902.

Nairn, I., Kobayashi, T. and Nakagawa, M., 1998, The ~10 ka multiple vent pyroclastic eruption sequence at Tongariro Volcanic Centre, Taupo Volcanic Zone, New Zealand: part 1. eruptive processes during regional extension, J. Volc. Geotherm. Res., 86, 19-44.

Nakano, M., and Kumagai, H., 2005, Waveform inversion of volcano-seismic signals assuming possible source geometries, Geophys. Res. Letts., 32, L12302.

Neuberg, J., Luckett, R., Baptie, B. and Olsen, K., 2000, Models of tremor and low-frequency earthquake swarms on Montserrat, J. Volc. Geotherm. Res., 101, 83-104.et al, 2000.

Ohminato, T., Chouet, B., Dawson, P. and Kedar, S., 1998, Waveform inversion of very-long-period implolsive signals associated with magmatic injection beneath Kilauea volcano, Hawaii, J. Geophys. Res., 103, B10, 23,839-23,862.

Robertsson, J., Blanch, J. and Symes, W., 1994, Visco-elastic finite-difference modelling, Geophysics, 59(9), 1444-1456.

Rowland, J.V. and Sibson, R.H., 2001, Extensional fault kinematics within the Taupo Volcanic Zone, New Zealand: soft linked segmentation of a continental rift system, N.Z J. Geol. Geophys., 44, 271-283.

Rowlands, D.P., White, R.S. and Haines, A.J., 2005, Seismic tomography of the Tongariro Volcanic Centre, New Zealand, Geophys. J. Int, 163, 1180-1194.

Tessmer, E., Kosloff, D. and Behle, A., 1992, Elsastic wave propagation simulation in the presence of surface topography, Geophys. J. Int., 108,621-632.

Turcotte, D.L., and Shubert, G., 1982, Geodynamics-Applications of Continuum Physics to Geological Problems, John Wiley and Sons.

Villamor, P. and Berryman, K. B., 2001, A late Quaternary extension rate in the Taupo Volcanic Zone, New Zealand, derived from fault slip data, N.Z J. Geol. Geophys., 44, 243-269.

Vireux, J., 1986, P-SV wave-propagation in heterogeneous media: velocity-stress finite-difference method, Geophysics, 51, 889-901.

TABLES

Table 1: Velocity model used for initial waveform inversion, Vp and Vs are primary and secondary wave velocities, rho is the density and Qp and Qs are the quality factors describing the attenuation of P and S waves respectively.

Layer	z(m)	Vp	Vs	rho	Qp	Qs
1	0000	3300	1850	2600	950	920
2	2000	3400	1910	2610	950	920
3	5000	4900	2750	2620	900	950
4	6000	5200	2920	2650	900	900

Table 2: Model used for low velocity test. Bold implies changes to the base model.

Layer	z(m)	Vp	Vs	rho	Qp	Qs
1	0000	**2500**	**1400**	2600	950	920
2	2000	3400	1910	2610	950	920
3	5000	4900	2750	2620	900	950
4	6000	5200	2920	2650	900	900

Table 3: Model used for attenuation tests. Bold implies changes to the base model.

Layer	z(m)	Vp	Vs	rho	Qp	Qs
1	0000	**2500**	**1400**	2600	**500**	**500**
2	2000	3400	1910	2610	**500**	**500**
3	5000	4900	2750	2620	**500**	**500**
4	6000	5200	2920	2650	**500**	**500**

Table 4: Model used for second waveform inversion. Bold implies changes to the base model.

Layer	z(m)	Vp	Vs	rho	Qp	Qs
1	0000	**2500**	**1400**	2600	**200**	**200**
2	2000	3400	1910	2610	**200**	**200**
3	5000	4900	2750	2620	**200**	**200**
4	6000	5200	2920	2650	**200**	**200**

Table 5: Model used for second waveform inversion. Bold implies changes to the base model.

Layer	z(m)	Vp	Vs	rho	Qp	Qs
1	0000	**2500**	**1400**	2600	**200**	**200**
2	2000	3400	1910	2610	**200**	**200**
3	5000	4900	2750	2620	**200**	**200**
4	6000	5200	2920	2650	**200**	**200**

Table 6: Velocity model used for second inversion. Bold implies changes to the base model.

Layer	z(m)	Vp	Vs	rho	Qp	Qs
1	0000	**2500**	**1400**	2600	**50**	**50**
2	2000	3400	1910	2610	**50**	**50**
3	5000	4900	2750	2620	**50**	**50**
4	6000	5200	2920	2650	**50**	**50**

Table 7: Parameters used for all Green's functions calculations.

15	Number of nodes for damping at boundaries
5	Number of Standard Linear Solids for modelling Q
0.5	Minimum frequency for attenuation
25.0	Maximum frequency for attenuation
2.0	Attenuation value for P-wave - ABS boundary
2.0	Attenuation value for S-wave - ABS boundary
8000.0	LATITUDE length of grid model (x direction, m)
8000.0	LONGITUDE length of grid model (y direction, m)
8000.0	height of the grid model in the (z direction, m)
100.0	space sampling in x direction (m)
100.0	space sampling in y direction (m)
50.0	space sampling in z direction (m)
-1500 to 1500	x position of source (m)
-1500 to 1500	y position of source (m)
500 to 1500	z position of source (m)
3.0	duration of the source (s)
6.0	computation duration (s)
0.005	numerical time step (s)
100.	sampling rate for seismograms output (Hz)

FIGURES

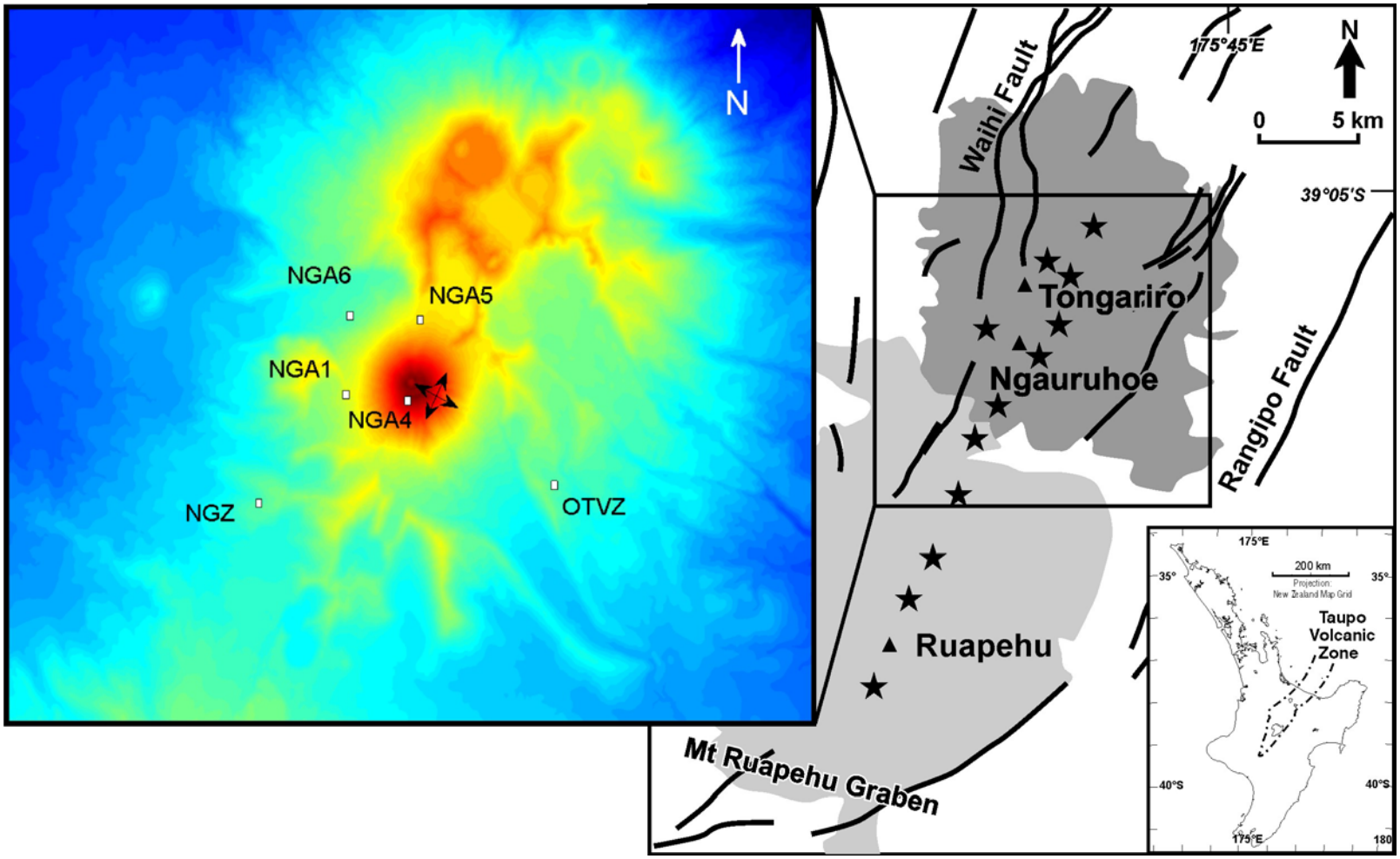

Figure 1: Location map of Ngauruhoe incorporating deposits of Tongariro (dark shading) and Ruapehu (light shading) and simplified fault structures (Grindley, 1960; Nairn et al., 1998; Rowland and Sibson, 2001; Villamor and Berryman, 2006). The triangles are volcano summits, while the stars are vents active about 10 ka years ago (so called 'PM' vents). The figure is modified after Cassidy et al. (2009). Topography and seismic stations used in modelling are shown (inset). Location of long-period source from modelling is shown as the double headed arrow in the inset.

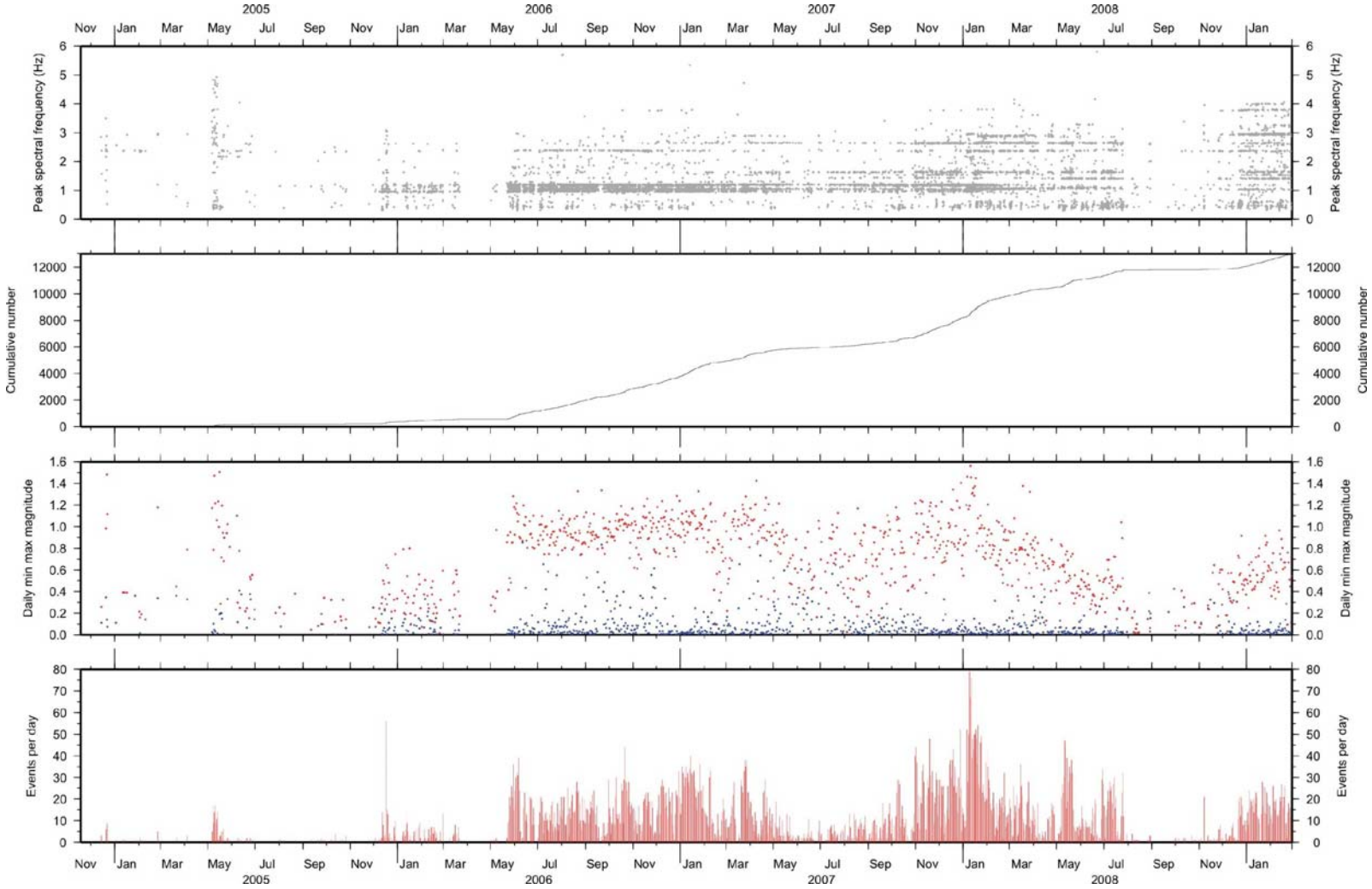

Figure 2: Time history of repeated earthquakes for Ngauruhoe. Panel 1 shows the peak spectral frequency (hz), panel 2 shows the cumulative number of earthquakes, panel three shows the peak and mean magnitude, panel 4 shows the daily number of earthquakes.

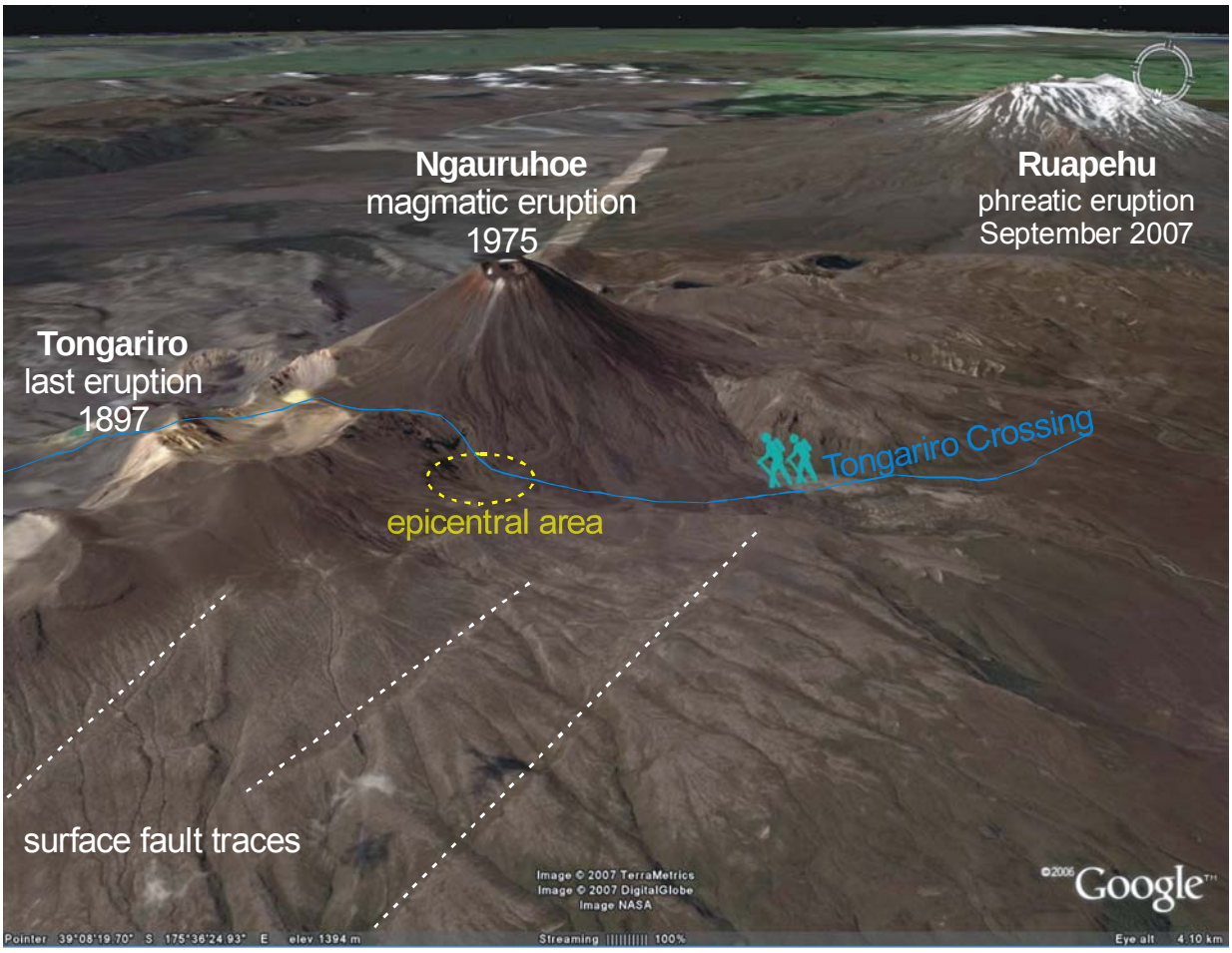

Figure 3: Approximate location of earthquakes based on first P arrivals to local network.

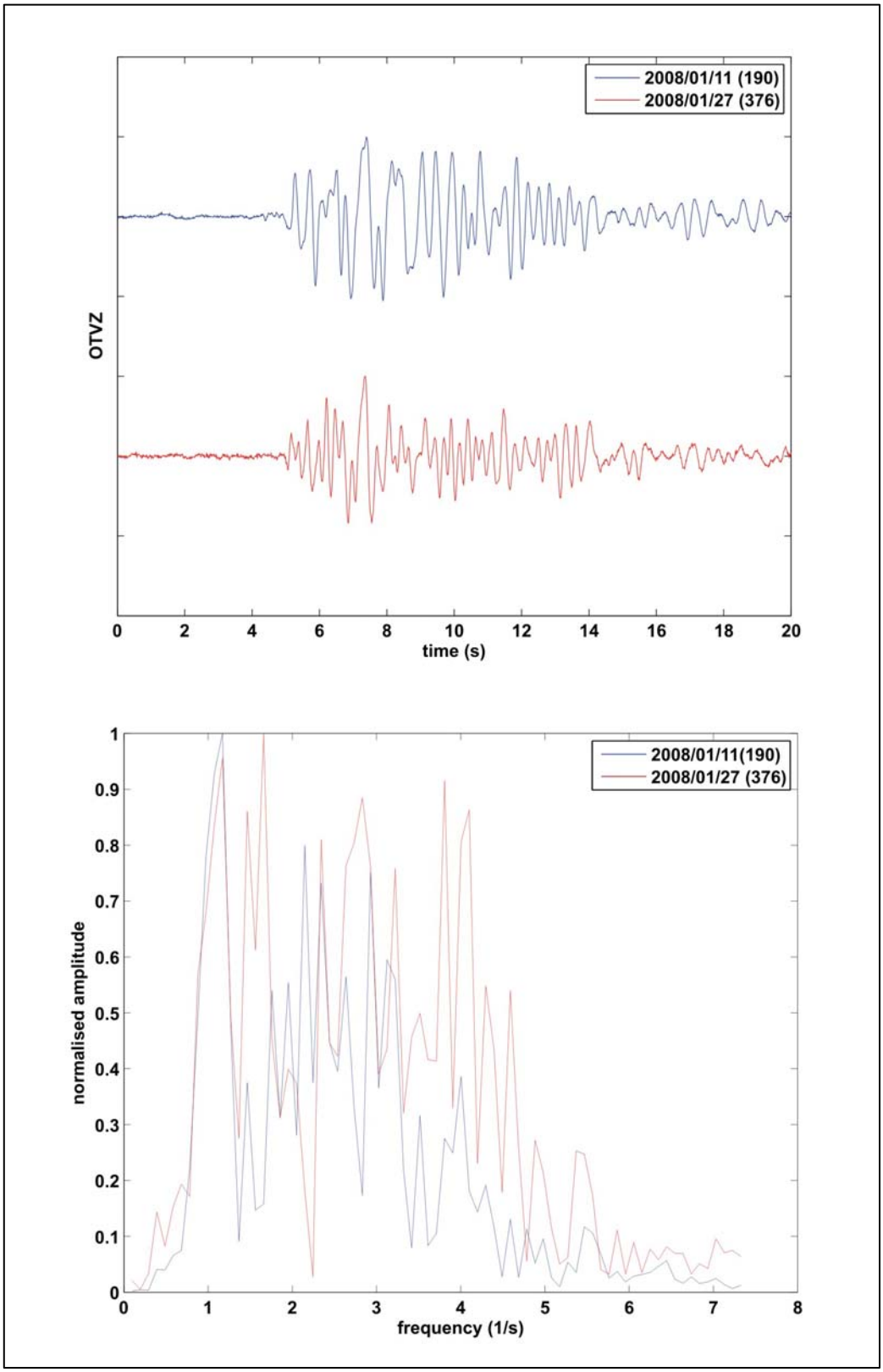

Figure 4: Example earthquakes recorded on 11 January and 27 January 2008 (top panel). The associated spectra are shown in the bottom panel. For both plots the amplitudes are normalised.

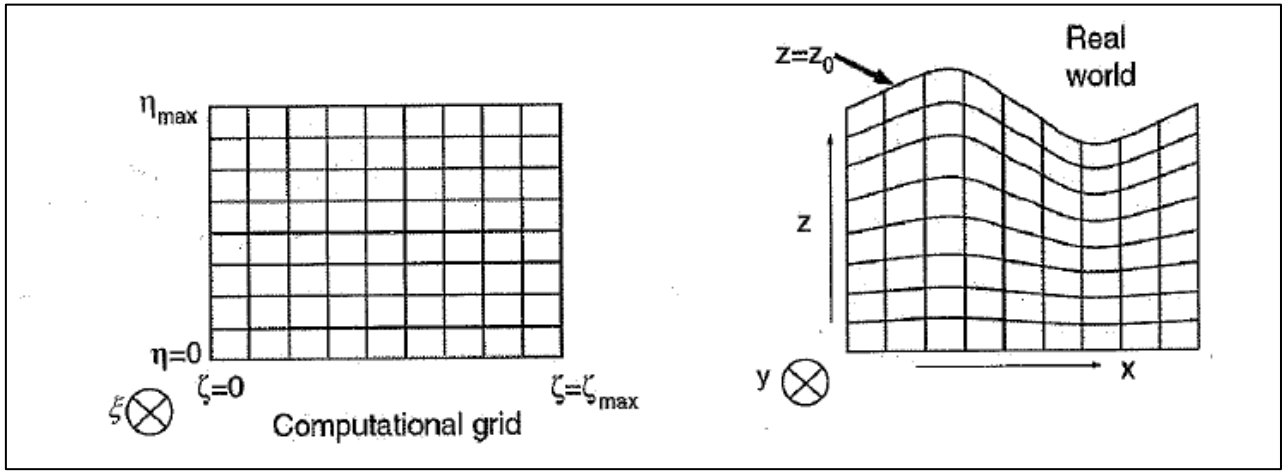

Figure 5: Curved grid in the (x,y,z) system and rectangular grid in the (ζ,ξ,η) system (Jousset et al, 2004).

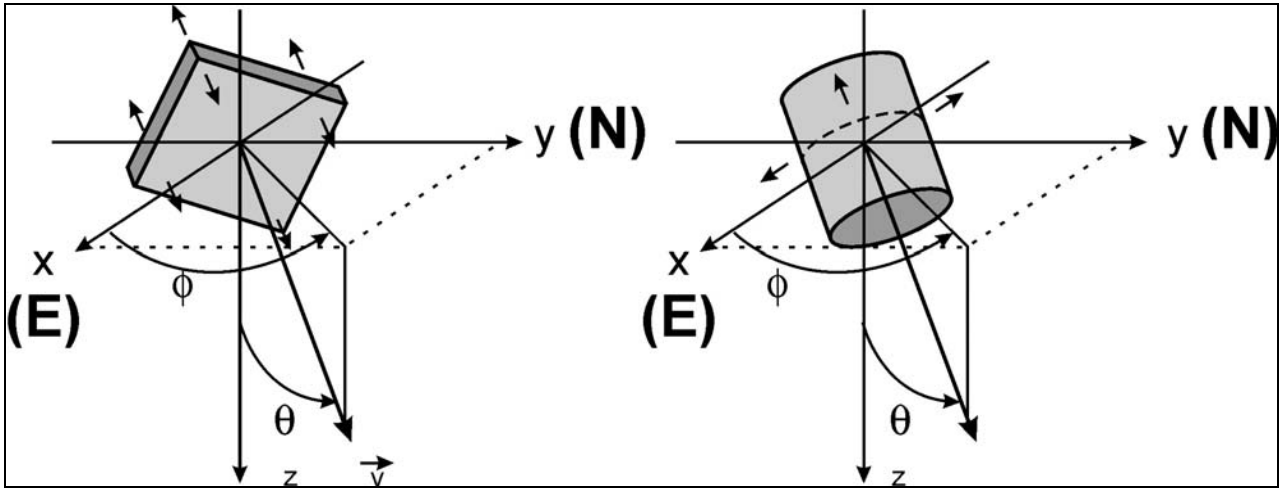

Figure 6: Coordinate system used for testing model geometries for Ngauruhoe volcano earthquakes. Model geometries include cracks (left) and pipes (right).

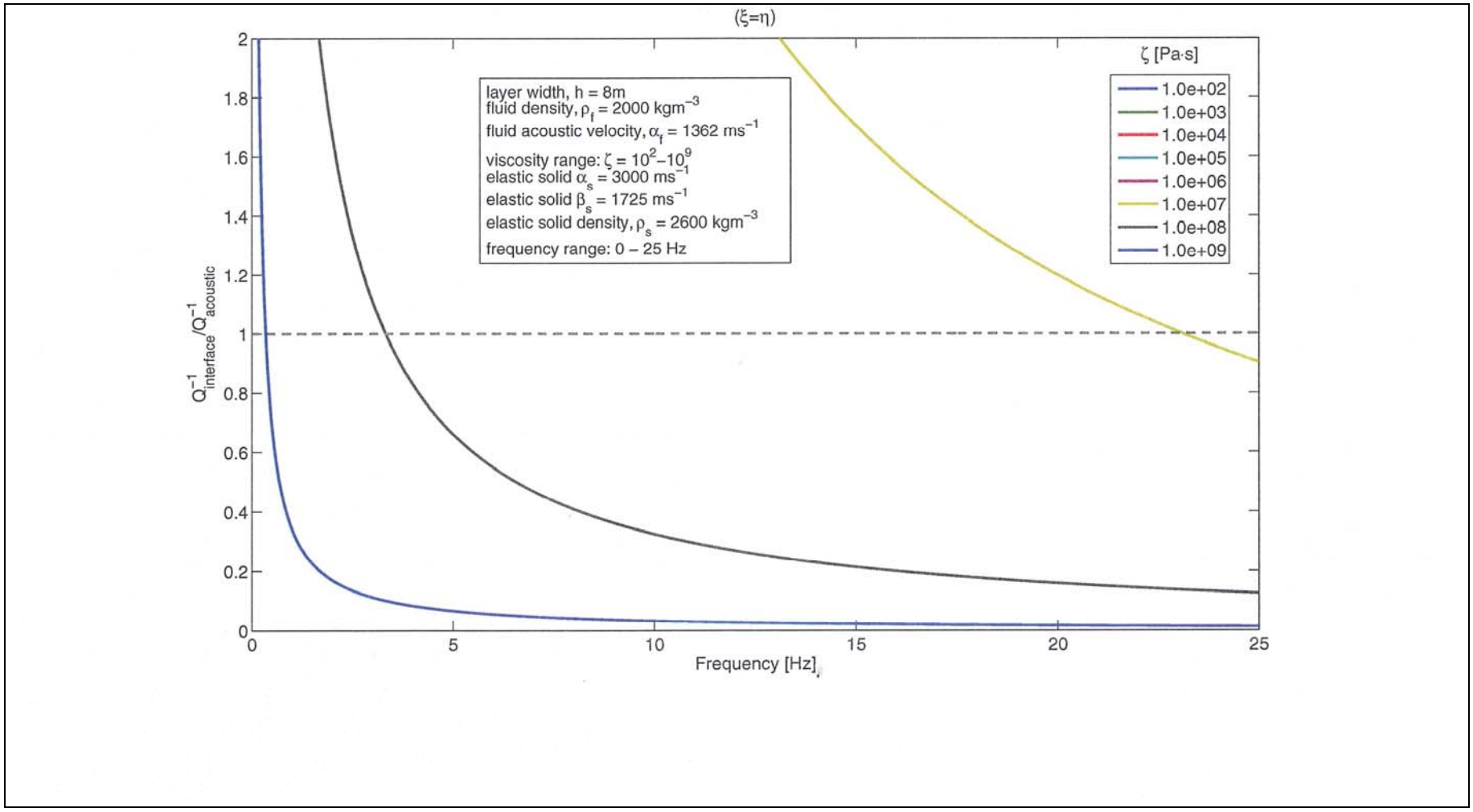

Figure 7: Ratio of interface wave attenuation to acoustic wave attenuation as a function of frequency for a range of viscosites. The inset box shows parameters used in the calculation.

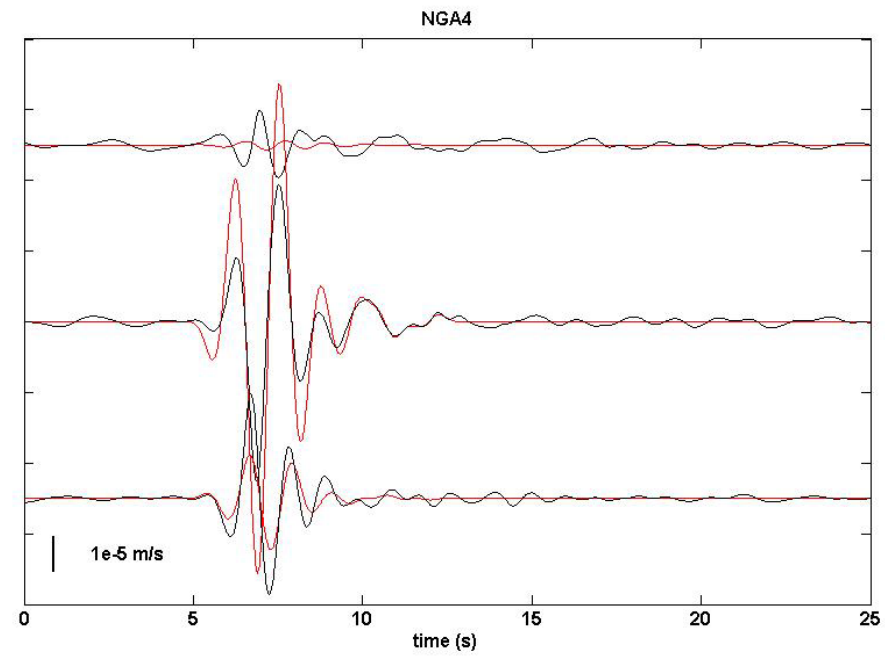

a)

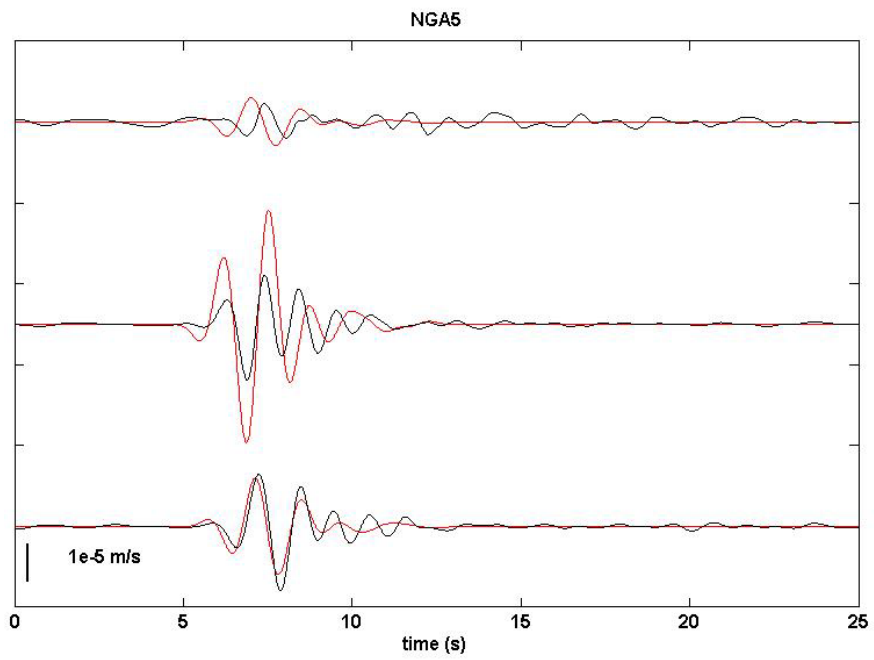

b)

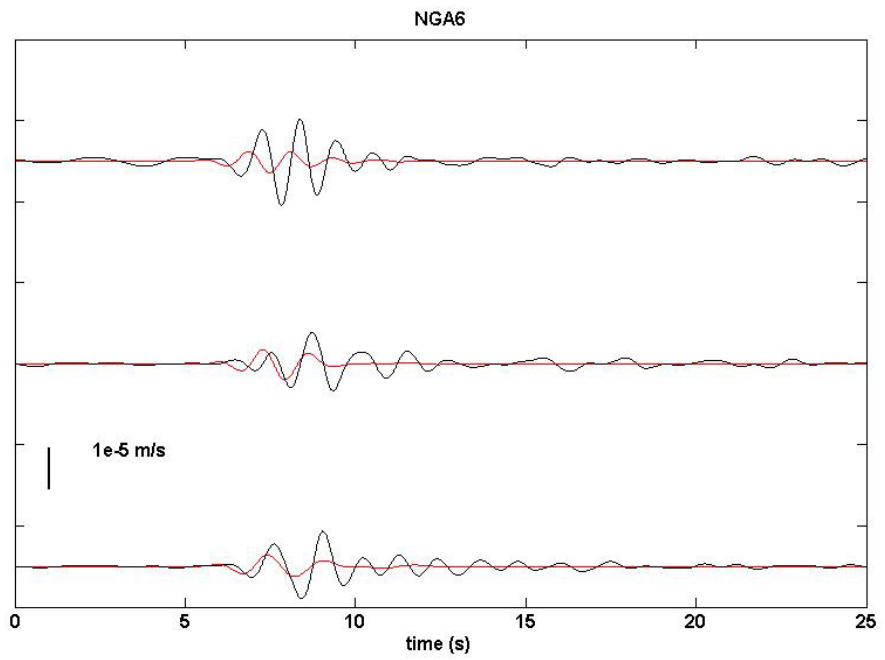

c)

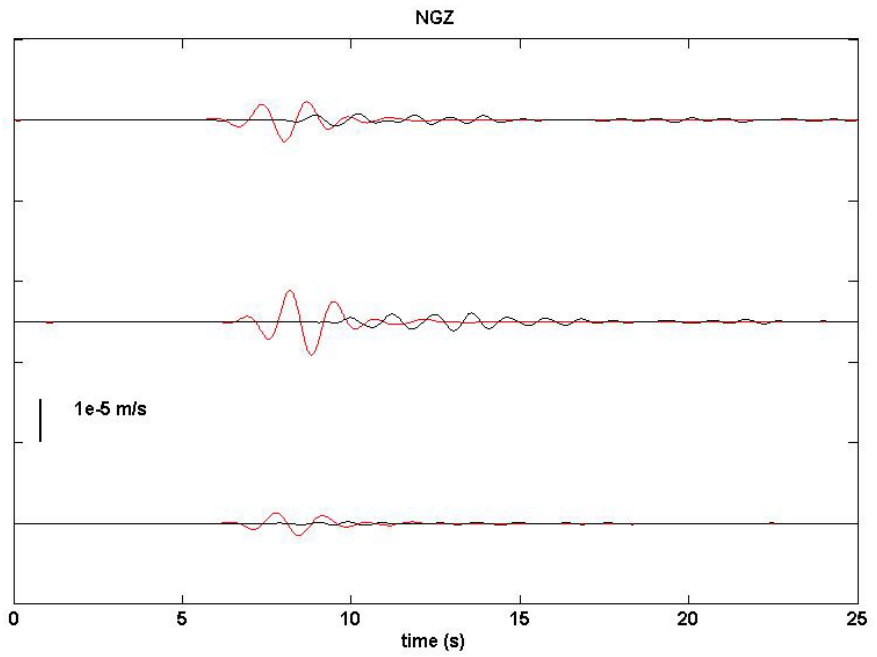

d)

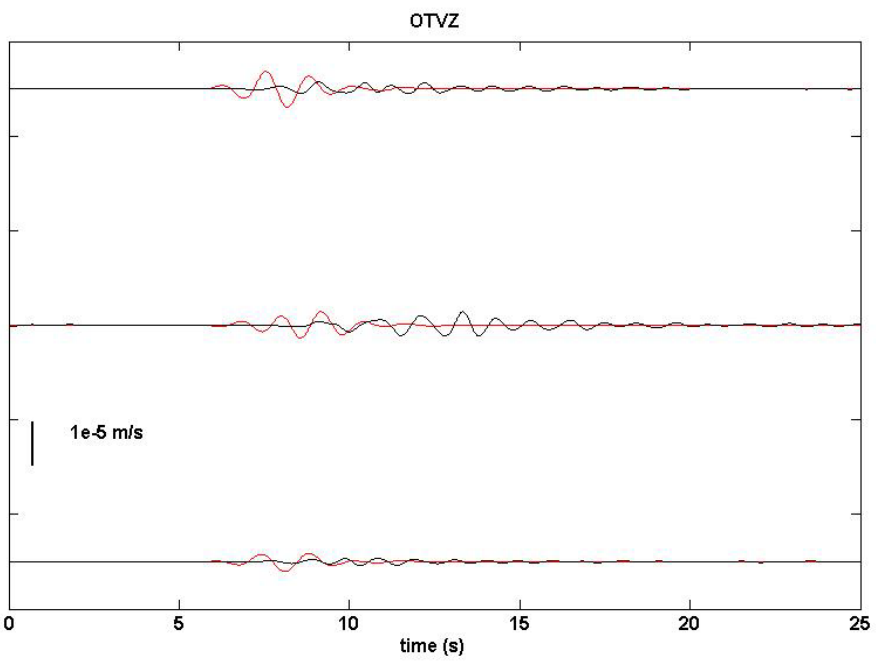

e)

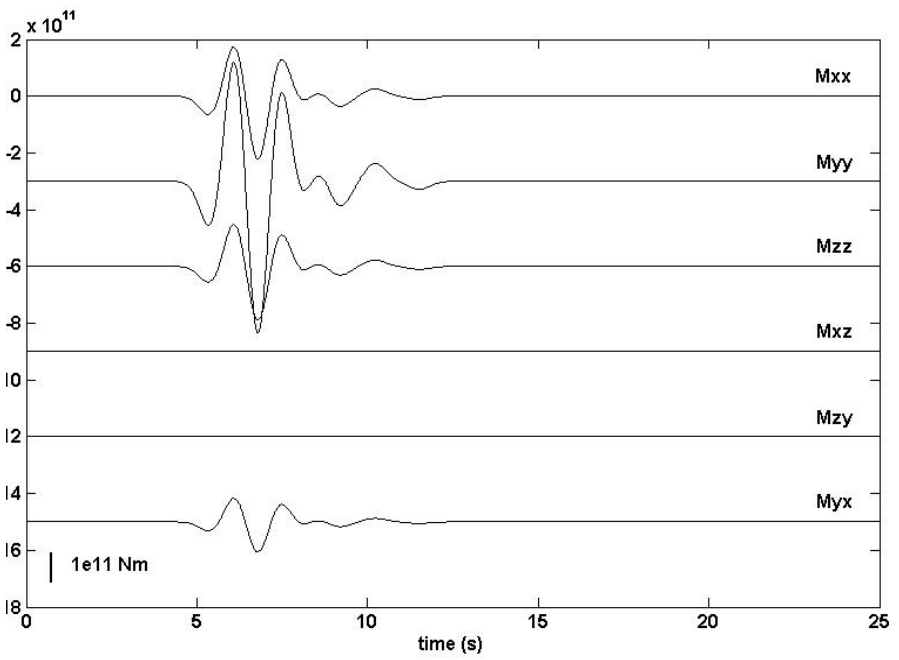

f)

Figure 8: Example model inversion results for N73°W crack (a,b,c,d.e) for earthquake recorded 17 January 2008 at 07:32 UT. The stations are temporary stations (NGA4,NGA5,NGA6) and permanent stations OTVZ and NGZ) (a-e), lines are observed data which are acausal filtered in the frequency band 0.33 to 1.0 Hz. The red lines show the inverted solutions for a N73°W vertically oriented crack. The inverted source moment components (f) was determined for a source located 200 m East, 100 m South and 800 m below the station NGA4 located at the Crater summit area (Figure 1). For each panel (a-e), the waveforms are (from top to bottom) North=positive, East=positive and Z up=positive components.

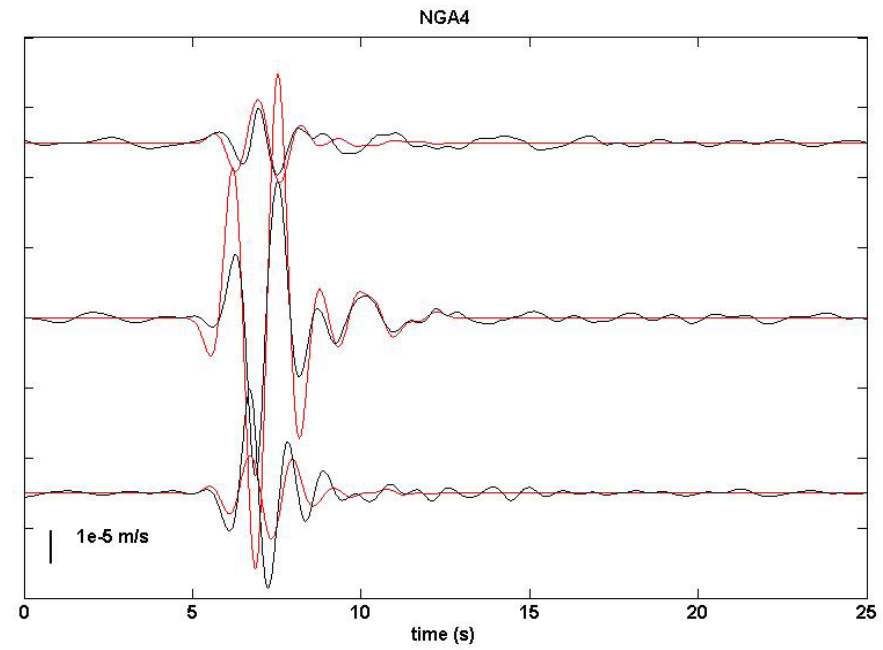

a)

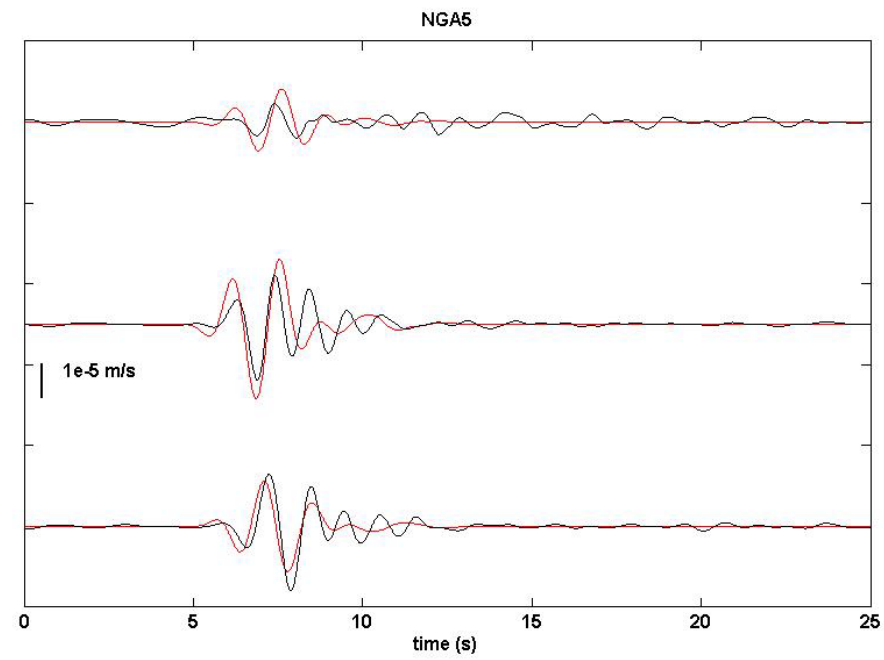

b)

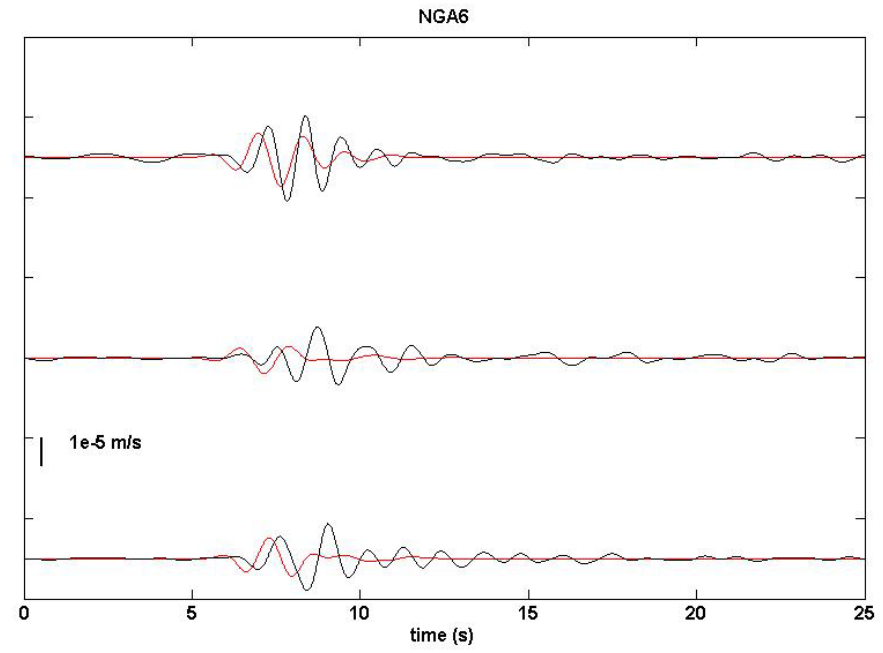

c)

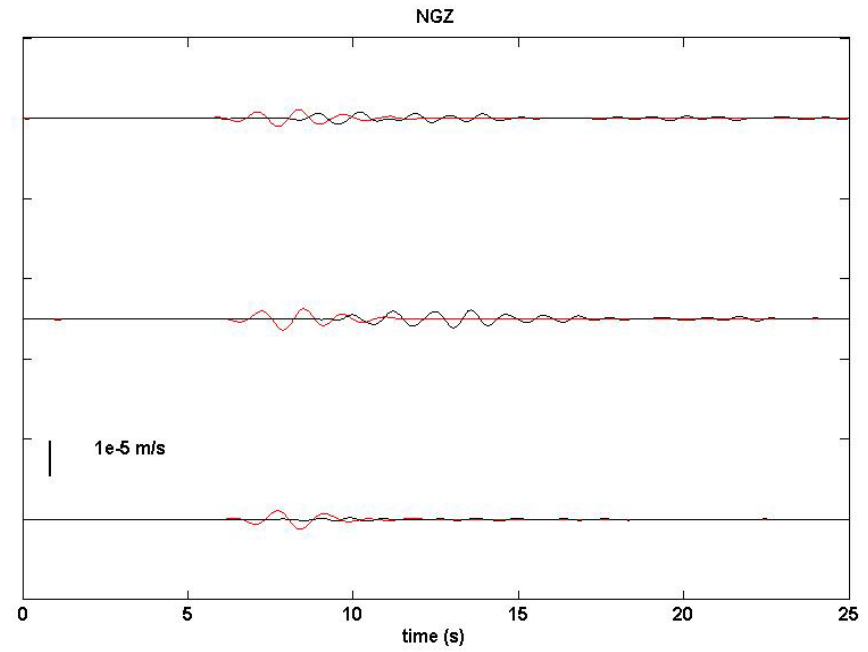

d)

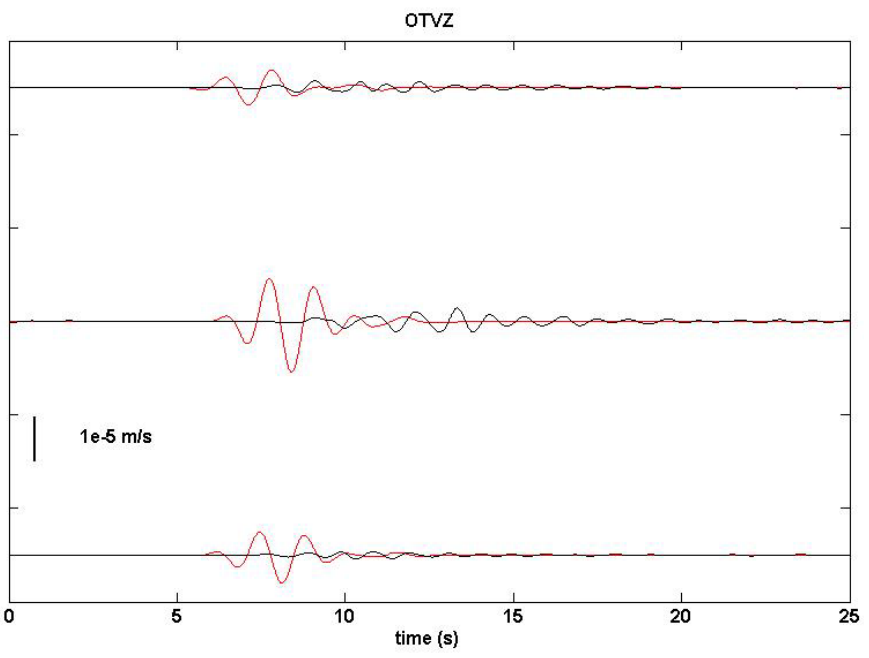

e)

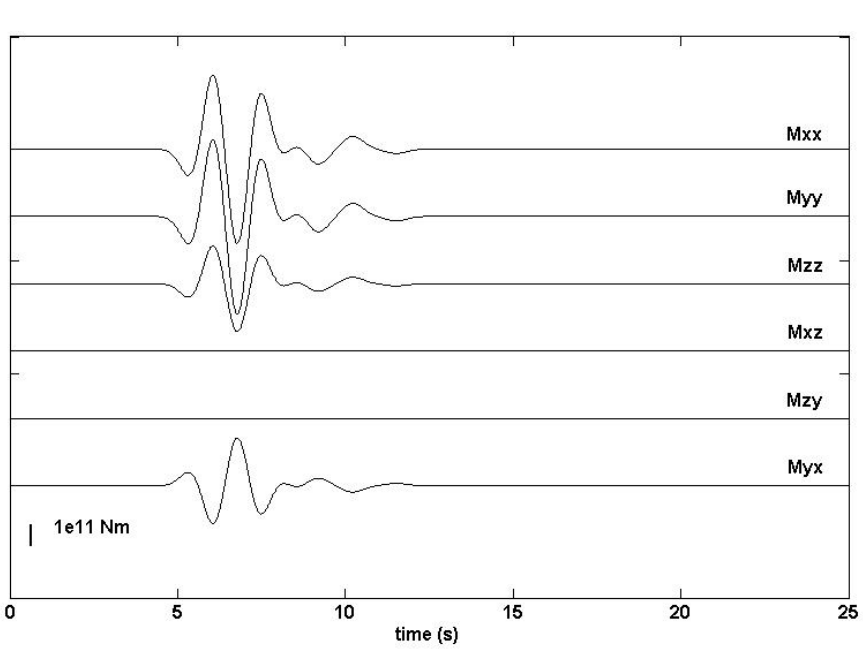

f)

Figure 9: Example model inversion results for N46^{o}E crack (a,b,c,d.e) and associated source time function (f). The inverted source time functions are dominated by volumetric components (M_{xx}, M_{yy}, M_{zz}) with lesser influence of shear component (M_{yx}). The inverted models in figure 8 and 9 are highly similar except for: 1) dominant amplitude for M_{yy} in N73^{o}W example (b) and the switch to M_{xx} dominance in N46^{o}E example (a) and: 2) polarity change observed for M_{yx} component seen in both panels. See Figure 8 for comparision.

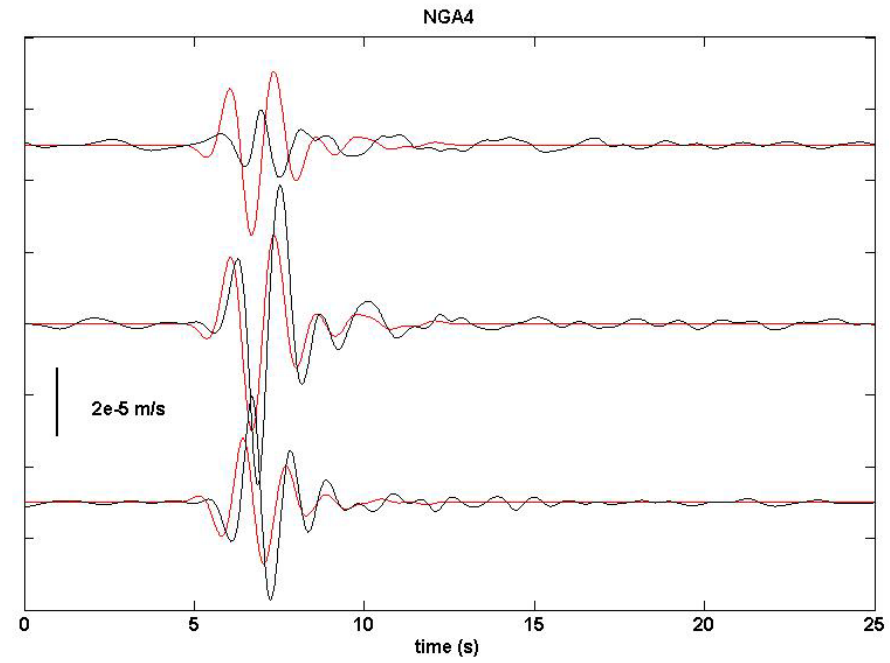

a)

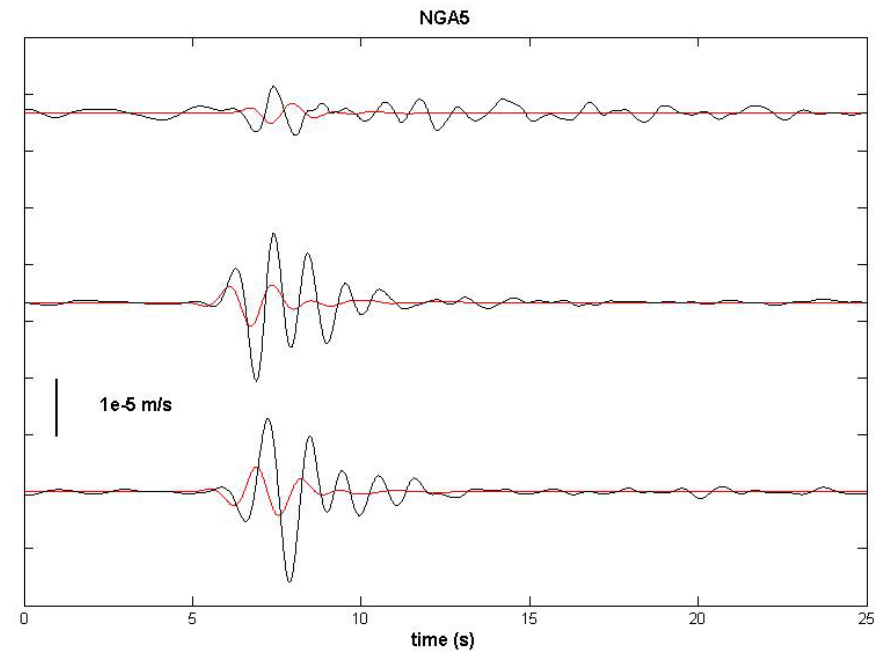

b)

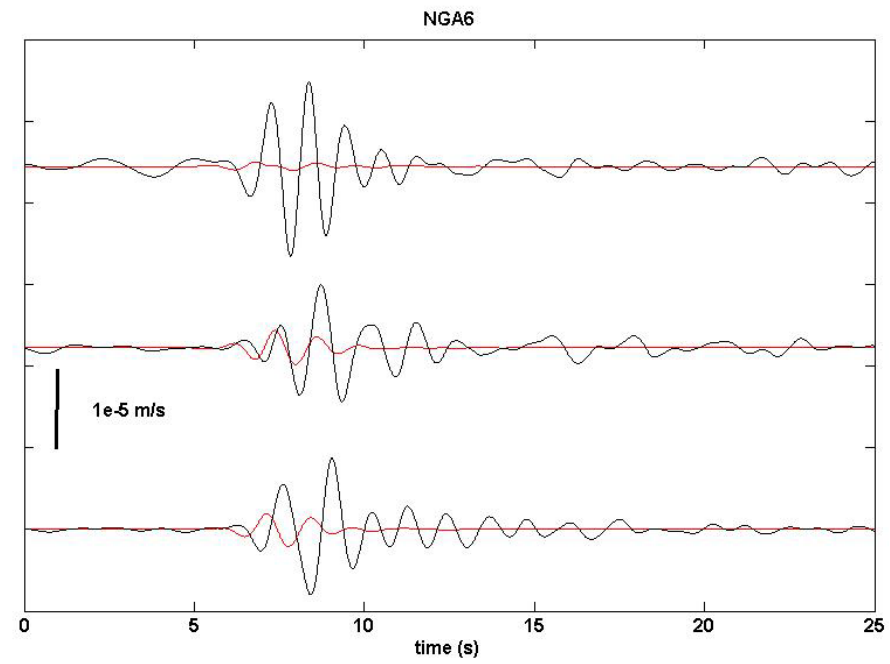

c)

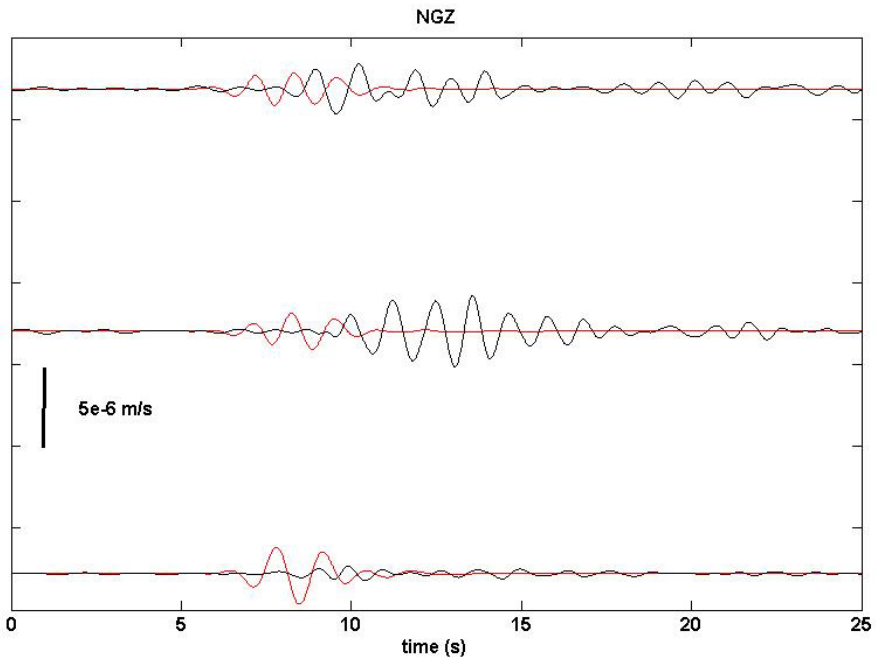

d)

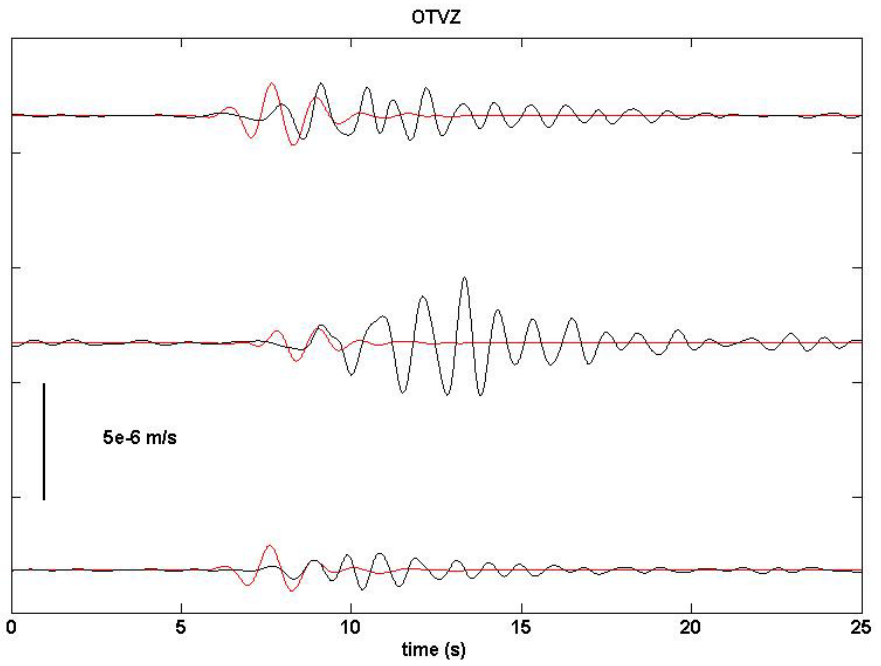

e)

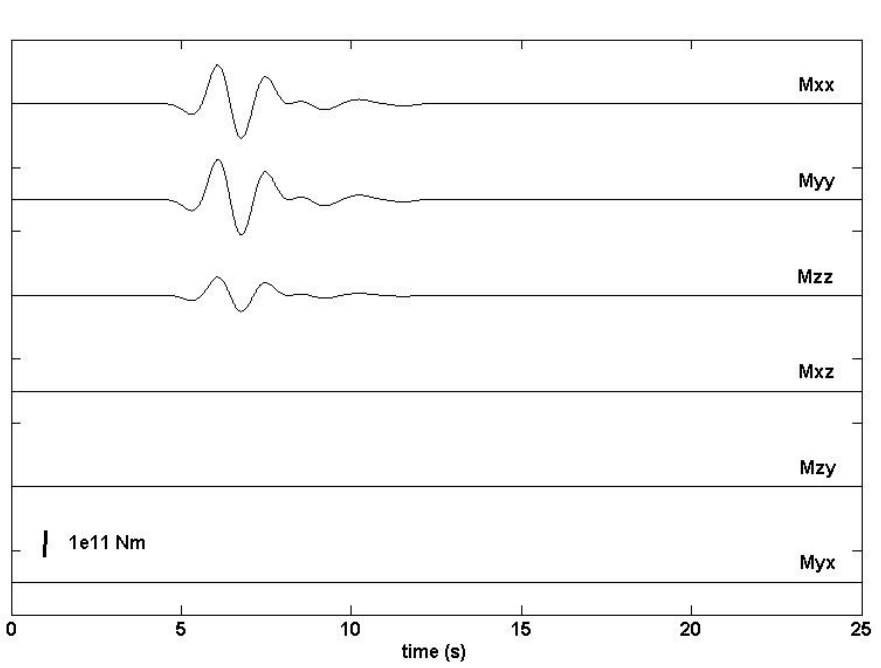

f)

Figure 10: Example inversion for vertical pipe model. The components are as described in Figure 8. Note that the source time function (f) is dominated by volumetric components (M_{xx},M_{yy},M_{zz}) with M_{xx},M_{yy} having twice amplitude of M_{zz} consistent with a [2,2,1] vertical pipe model.

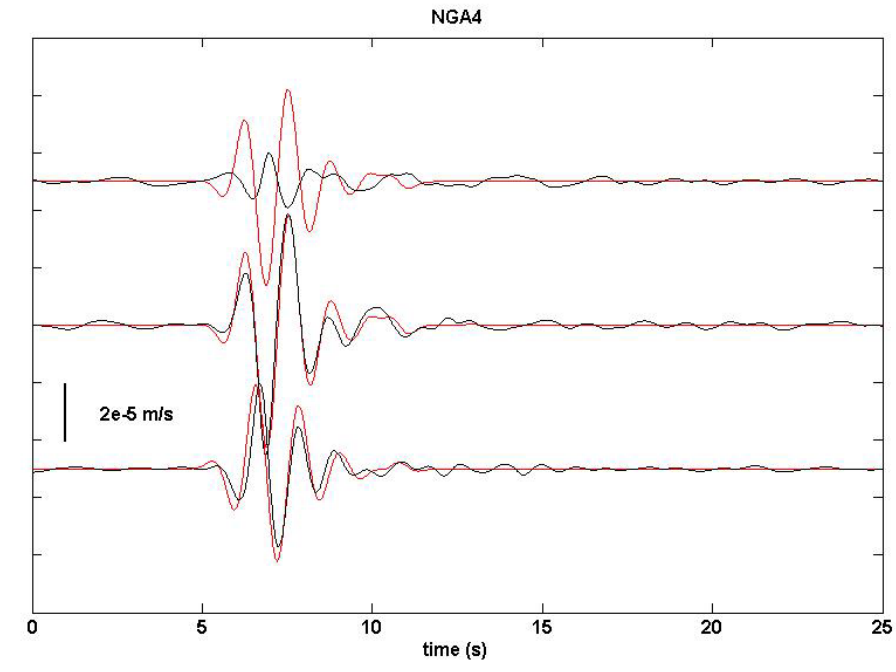

a)

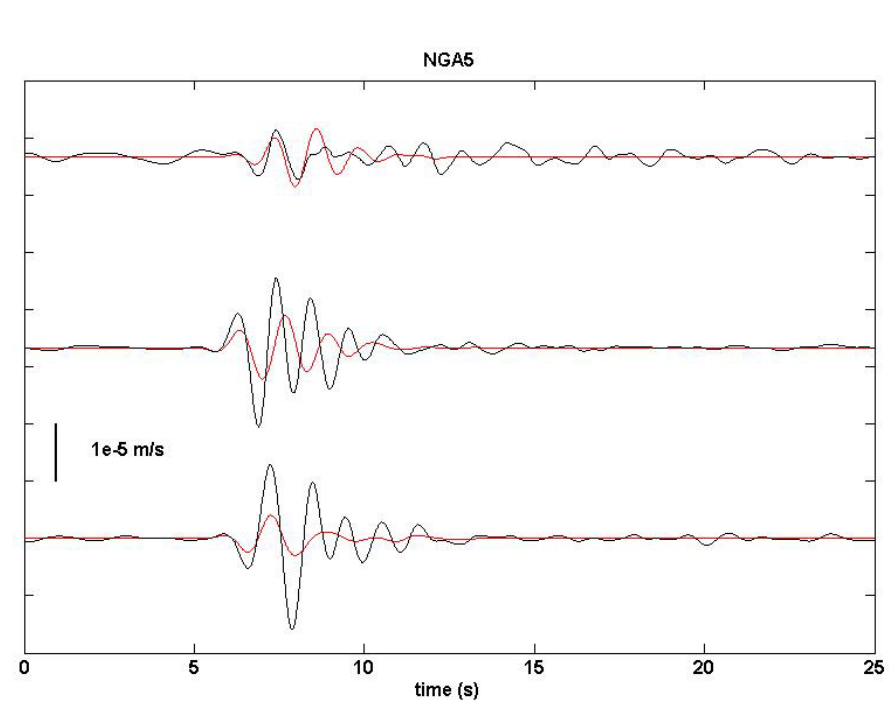

b)

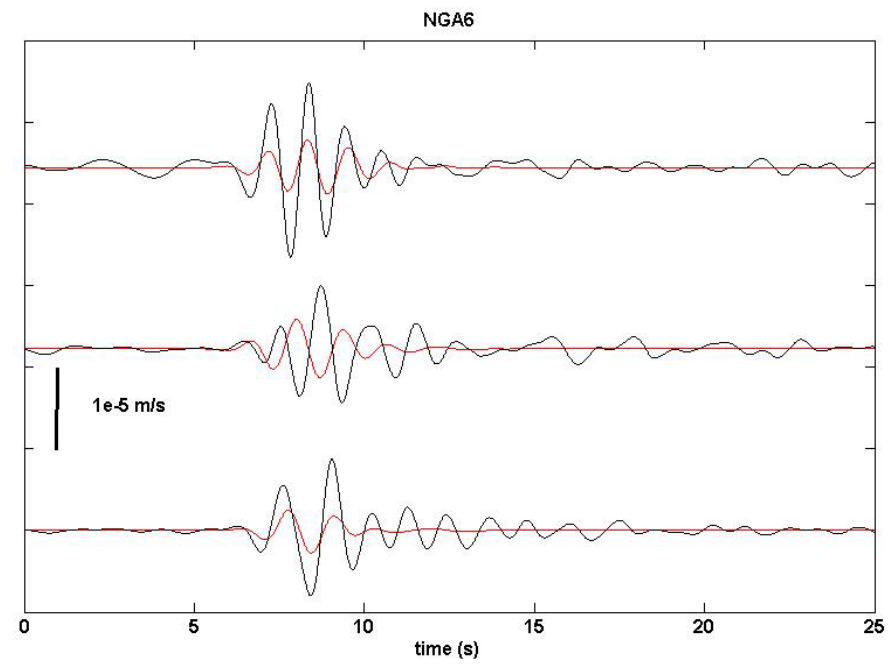

c)

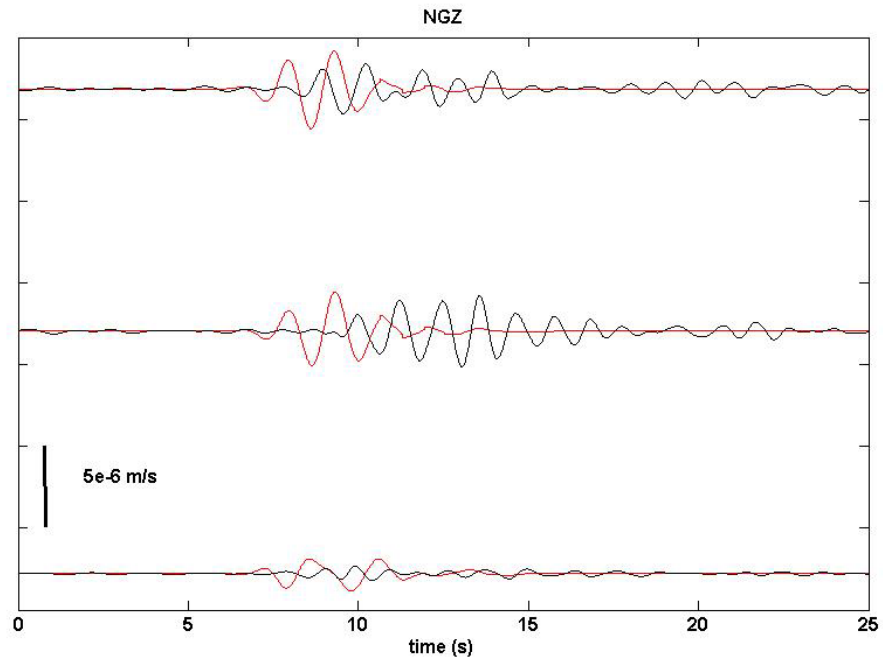

d)

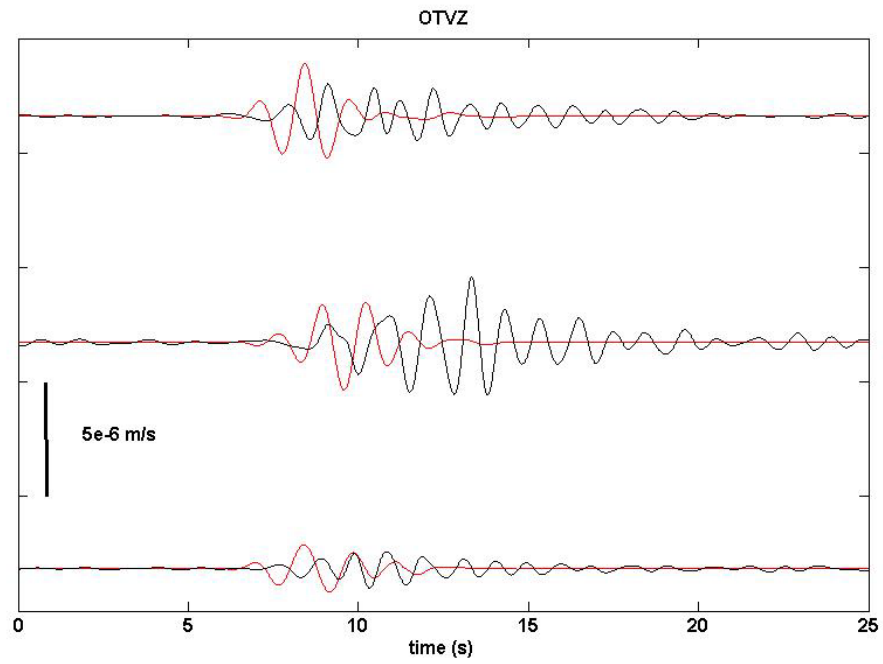

e)

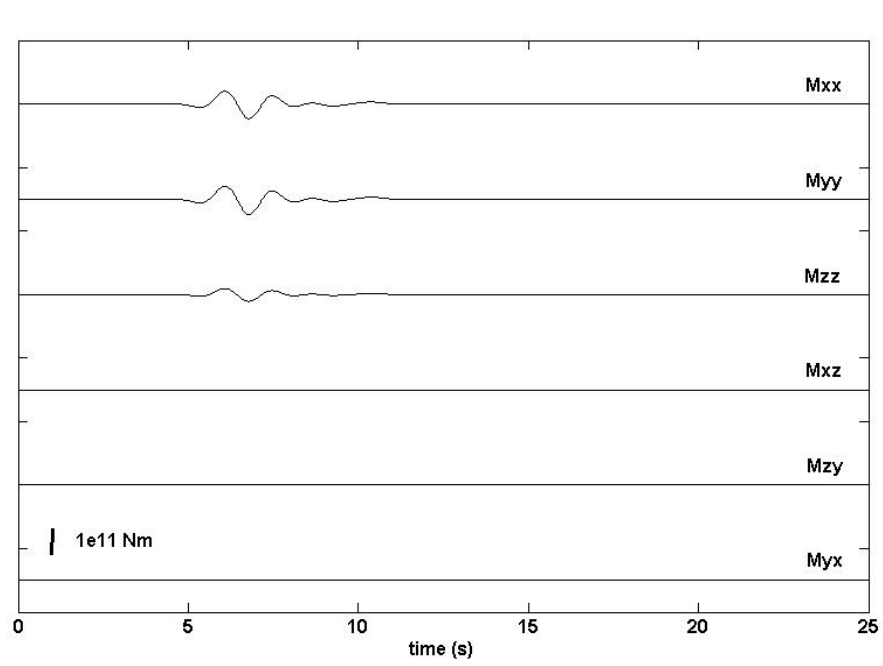

f)

Figure 11: Effects of an alternative velocity model (Table 2) on waveform inversion results. See Figure 10 for comparison to the base model (Table1). For both Figure 10 and 11 we show the vertical pipe model.

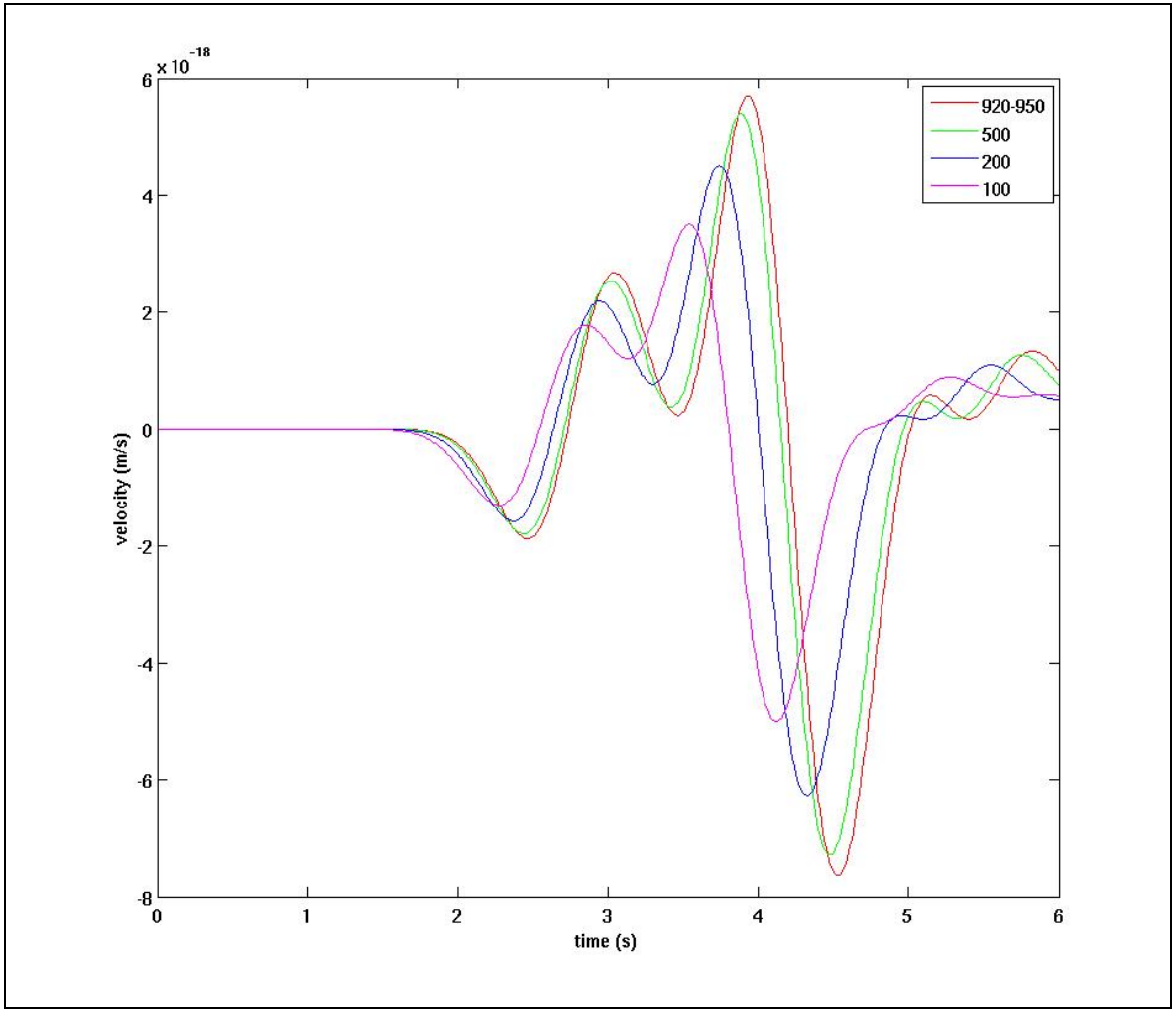

Figure 12: Synthetic waveforms for an explosive source observed at station NGZ for various damping values (Q). The model run variations are from Tables 2-5. Note the changes in phase arrival time and maximum amplitude.

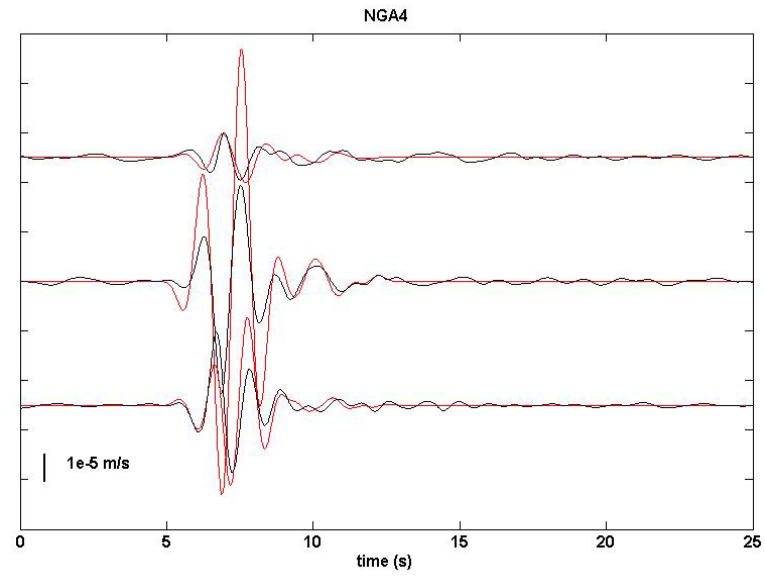

a)

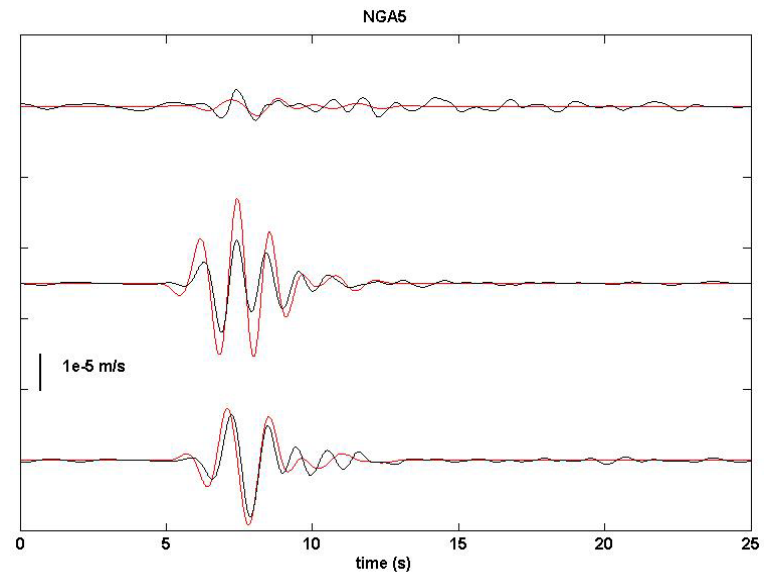

b)

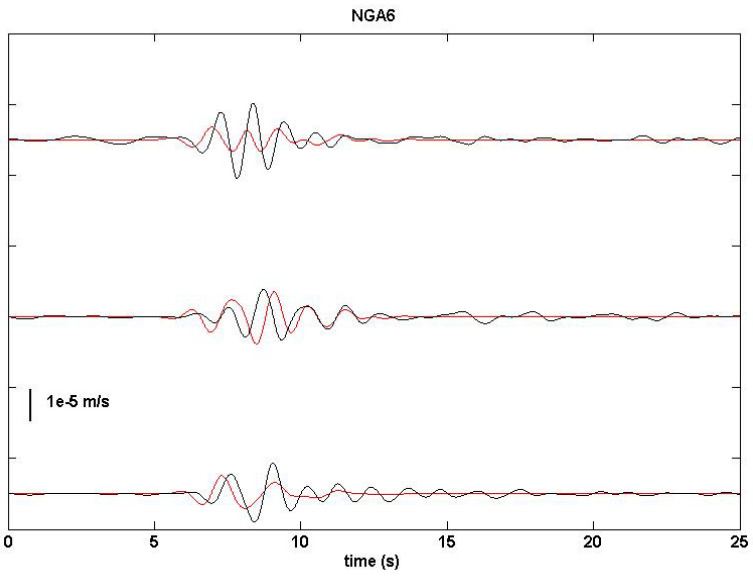

c)

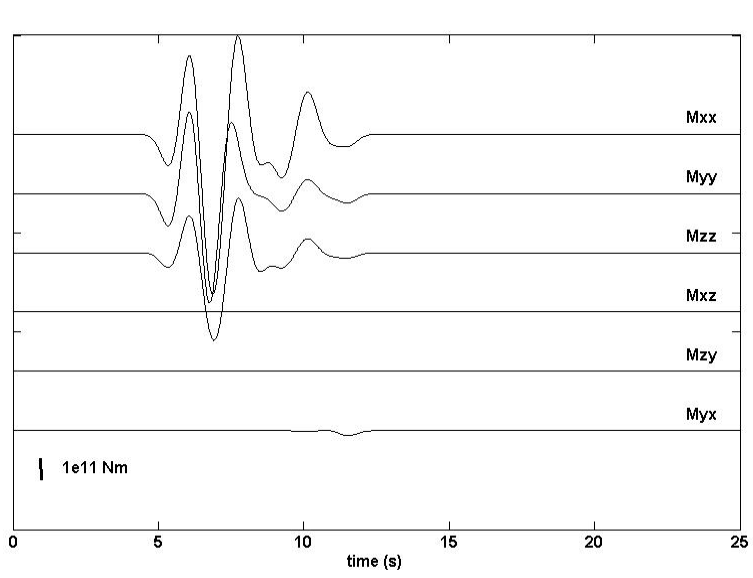

d)

Figure 13: Inversion result for a time-varying source model. Waveform matches are shown for NGA4 (a), NGA5 (b) and NGA6 (c). The associated source time function is shown in (d).

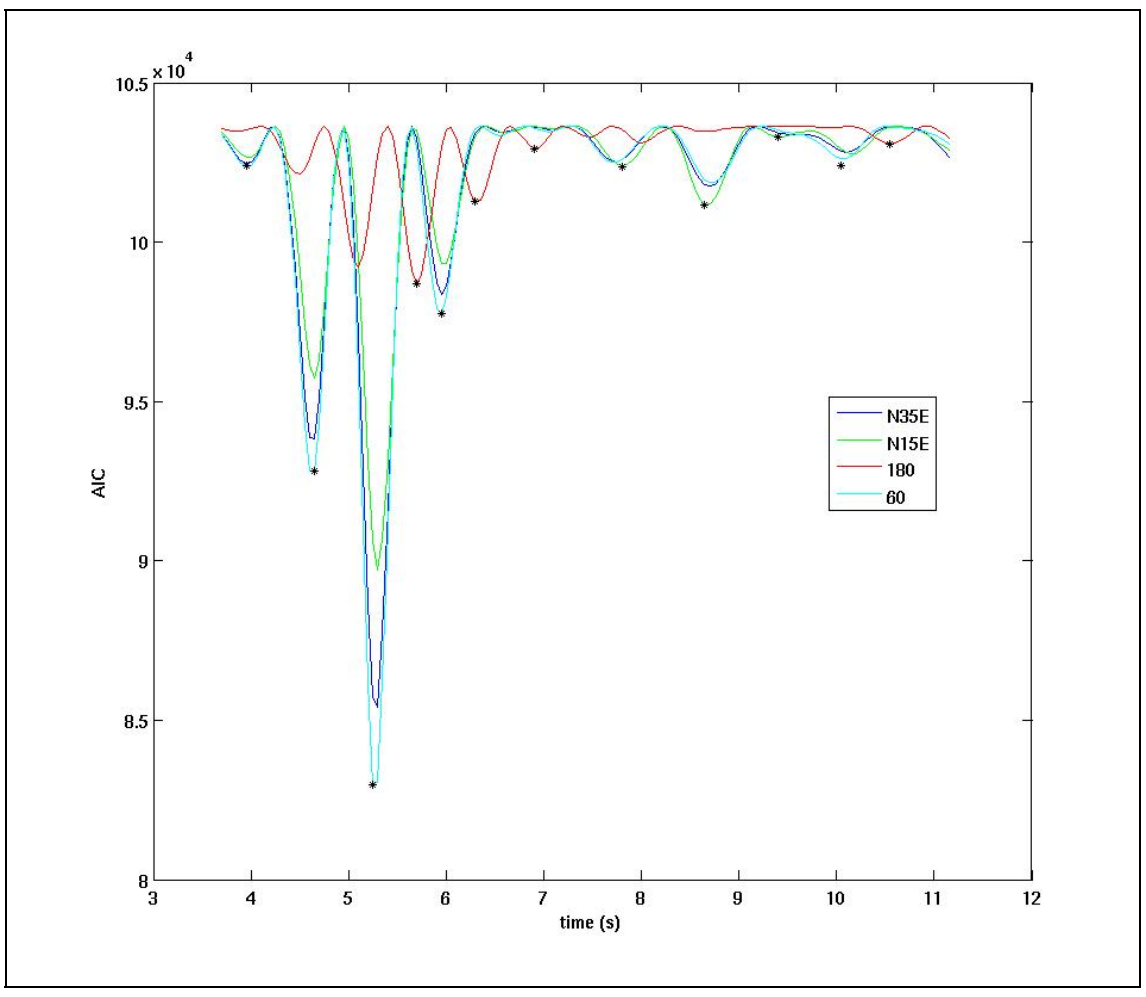

Figure 14: Model fits with time for source time functions shown in Figure 13. The black stars show the points where the error is minimised. This minima, given by the AIC discussed in section 2.3, is the best model of all geometries tested at the particular time period. Example models shown include N35^{o}E oriented vertical crack (blue), a N15^{o}E crack (green), a vertical pipe having φ=180^{o} (red), and a vertical pipe having φ = 60^{o} (cyan). Not all models are shown in this figure, hence the minimum model given by the black stars may not be shown in the examples. Time for this figure is relative to the start of the synthetic window compared to the observed traces and not the time associated with the waveform matches shown in Figure 13.

www.gns.cri.nz

Principal Location

1 Fairway Drive
Avalon
PO Box 30368
Lower Hutt
New Zealand
T +64-4-570 1444
F +64-4-570 4600

Other Locations

Dunedin Research Centre
764 Cumberland Street
Private Bag 1930
Dunedin
New Zealand
T +64-3-477 4050
F +64-3-477 5232

Wairakei Research Centre
114 Karetoto Road
Wairakei
Private Bag 2000, Taupo
New Zealand
T +64-7-374 8211
F +64-7-374 8199

National Isotope Centre
30 Gracefield Road
PO Box 31312
Lower Hutt
New Zealand
T +64-4-570 1444
F +64-4-570 4657